Journal of Sound and Vibration 332 (2013) 3438–3462

Contents lists available at SciVerse ScienceDirect

Journal of Sound and Vibration

journal homepage: www.elsevier.com/locate/jsvi

Damage visualization based on local dynamic perturbation: Theory and application to characterization of multi-damage in a plane structure

Hao Xu [a,b], Li Cheng [a,b], Zhongqing Su [b,*], Jean-Louis Guyader [c]

[a] The Hong Kong Polytechnic University Shenzhen Research Institute, Shenzhen 518057, PR China
[b] The Department of Mechanical Engineering, The Hong Kong Polytechnic University, Kowloon, Hong Kong, Special Administrative Region
[c] Laboratoire Vibrations Acoustique, Institut National des Sciences Appliquées (INSA), de Lyon 69621, Villeurbanne, France

ARTICLE INFO

Article history:
Received 29 May 2012
Received in revised form
14 January 2013
Accepted 25 January 2013
Handling Editor: I. Trendafilova
Available online 15 March 2013

ABSTRACT

Previously, an inverse damage characterization framework was proposed by quantifying the perturbation to local dynamic equilibrium of a beam-like structure, showing advantages in some aspects over the traditional global vibration-based and local guided-wave-based methods. Residing on the plate theory, this framework was expanded to a two-dimensional domain. Inheriting the attributes of localized canvassing using high-order spatial derivatives this approach has proven effectiveness in quantitatively characterizing damage of small dimension, regardless of its number and type. In addition, the approach requires no benchmarks, baseline signals, global models, additional excitation sources, pre-modal analysis nor prior knowledge on structural boundary. A damage imaging algorithm using the quantified dynamic perturbation was further established, enabling presentation of damage characterization results in an intuitive and prompt manner. Integrating the detection capacities in one- and two-dimensional domains, a hybrid damage visualization strategy was developed, for systems comprising structural components of different types, various geometries and diverse boundary conditions. Two independent de-noising techniques (low-pass wavenumber filtering and adjustment of measurement density), together with a hybrid data fusion algorithm, were proposed as auxiliary means to enhance the robustness of the strategy in noisy measurement conditions. The strategy was applied experimentally to the evaluation of multi-damage in a plane structure comprising beam and plate components, showing satisfactory results.

1. Introduction

By perceiving and quantifying the perturbation to local dynamic equilibrium of a beam-like structure, a damage characterization framework was developed in authors' previous work [1]. The underlying philosophy behind is that a beam component satisfies, locally at its every single fragment, a sort of dynamic equilibrium conditions (*e.g.*, equation of motion). Upon occurrence of damage, such equilibrium is disturbed at the fragments with damage, manifesting as certain changes in the captured dynamic responses; in turn, this perturbation, if detected properly, can indicate the damage

* Corresponding author. Tel.: +852 2766 7818; fax: +852 2365 4703.
E-mail address: mmsu@polyu.edu.hk (Z. Su).

0022-460X/$ - see front matter © 2013 Elsevier Ltd. All rights reserved.
http://dx.doi.org/10.1016/j.jsv.2013.01.033

occurrence. Development of the framework was largely motivated by the recognition of some obvious deficiencies of the currently prevailing nondestructive evaluation techniques [2,3] based on either changes in global properties of structural vibration [4] (*e.g.*, eigen-frequencies [5–7], mode shape [8,9], modal curvature [9,10], electro-mechanical impedance [11], flexibility matrix [12–14] and damping properties [15]) or abnormity in local characteristics of guided waves (*e.g.*, plate waves [16–23]). Although recent technical breakthroughs such as three-dimensional laser scanning vibrometry and advanced signal processing have retrofitted conventional global vibration-based or local guided-wave-based detection with the use of sparse piezoelectric sensor network [24–26], that proposed framework has been demonstrated to have, compared with conventional approaches:

(1) higher sensitivity to damage of small dimension, owing to the use of higher-order equation of motion (global properties can be insensitive to damage before it reaches a conspicuous extent; guided waves can suffer from the wavelength of a selected mode);
(2) capability of local interrogation in accordance with a point-by-point inspection manner (theoretically it can be infinitesimal), thus independent of a global model;
(3) no need of prior information on structural boundaries (*viz.*, complexity of a system would not downgrade the applicability of the approach) nor request of modal analysis (*i.e.*, a deliberately generated mode shape of the system is not of necessity);
(4) no prerequisite for benchmark structures nor baseline signals, therefore immune from the interferences of fluctuating environment conditions (*e.g.*, temperature variation);
(5) insensitivity to sensor arrangement (in guided wave-based detection, meticulous and strategic arrangement of sensor/actuator is often required); and
(6) applicability to detection of multi-damage, regardless of the damage type and number, thanks to the nature of local canvassing.

This framework was developed based on the theory of Euler–Bernoulli beam, and its applicability to two-dimensional structural components (*e.g.*, plates or shells) and more complex systems warrants further investigation. In this study, based on the plate theory, this framework was projected to a two-dimensional domain for plate-like structural components. Sharing the same rationale, all the merits enumerated in the above are inherited. To present damage characterization results in an intuitive way, a damage imaging algorithm was introduced, whereby detailed depiction of the damage (*e.g.*, number, shape and size) can directly be observed in constructed images. Combining the detection capacities in one- and two-dimensional domains, a hybrid damage visualization strategy was established for systems comprising structural components of different types, various geometric parameters and diverse boundary conditions. In addition, envisaging possible susceptibility of the approach to measurement noise (due to the involvement of higher-order derivatives), two independent de-noising techniques (low-pass wavenumber filtering and adjustment of measurement density), along with a hybrid data fusion algorithm, were proposed, to enhance noise immunity of the approach in practical implementation. The strategy was then applied experimentally to the evaluation of multi-damage in a plane structure comprising beam and plate components.

2. Rationale

In authors' previous study [1], a one-dimensional damage index (DI) for a beam-like component was derived based on the Euler–Bernoulli beam theory, by quantifying the perturbation to local dynamic equilibrium of the beam, which is defined as

$$\mathrm{DI} = EI\frac{d^4w(x)}{dx^4} - \rho S\omega^2 w(x), \tag{1}$$

where $w(x)$ is the flexural displacement of the beam at location x along the beam span when the beam vibrates at an angular frequency of ω ; E, ρ, I, and S are the complex modulus of elasticity (comprehending material damping), density, cross-sectional moment of inertia and area of the cross-section for a pristine beam, respectively. Both theoretical analysis and numerical validation have demonstrated that DI presents drastic changes on damage boundaries as a result of the discontinuity in material and geometric properties therein. Thus, DI can serve as an indicator of the presence of damage.

Likewise, a two-dimensional damage index can be derived based on the plate theory for a plate-like component bearing a damaged zone (Θ), as shown schematically in Fig. 1(a). Irrespective of the boundary conditions, the local dynamic equilibrium of a fragment extracted from the plate component (infinitesimal in principle), as shown in Fig. 1(b), with a homogeneous and isotropic material nature, can be expressed in a harmonic regime, in terms of the internal moments and external load applied to this fragment, as [27]

$$\left[-\frac{\partial^2}{\partial x^2}M_x(x,y) - 2\frac{\partial^2}{\partial x\partial y}M_{xy}(x,y) - \frac{\partial^2}{\partial y^2}M_y(x,y)\right] - \rho h\,\omega^2 w(x,y) = q(x,y), \tag{2}$$

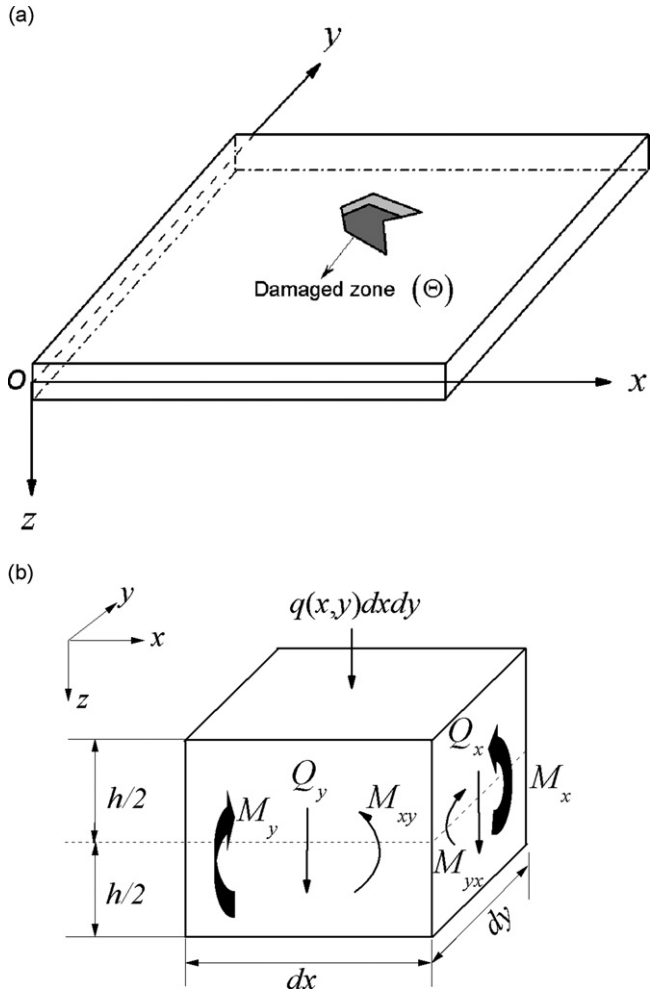

Fig. 1. Schematics of (a) a plate component bearing a damaged zone and (b) a fragment extracted from the component shown in (a) with internal forces and moments.

where

$$M_x(x,y) = -D\left(\frac{\partial^2 w(x,y)}{\partial x^2} + v\frac{\partial^2 w(x,y)}{\partial y^2}\right), \tag{3a}$$

$$M_y(x,y) = -D\left(\frac{\partial^2 w(x,y)}{\partial y^2} + v\frac{\partial^2 w(x,y)}{\partial x^2}\right), \tag{3b}$$

$$M_{xy}(x,y) = -D(1-v)\frac{\partial^2 w(x,y)}{\partial x \partial y} \tag{3c}$$

In the above (as indicated in Fig. 1(b)), $M_x(x,y)$ and $M_y(x,y)$ are the internal bending moments with regard to x- and y-axes, respectively; $M_{xy}(x,y)$ and $M_{yx}(x,y)$ ($M_{xy}(x,y) = M_{yx}(x,y)$) are the internal torsion moments. $w(x,y)$ is the flexural displacement of the plate fragment at (x,y) when it undergoes a steady vibration with an angular frequency of ω, which can, for example, be the 'natural excitation' incurred from the normal operation of the system or an ambient excitation. In the case that a 'natural excitation' is not harmonic, a frequency component in the frequency domain after Fourier Transform can be selected. h and ρ represent the thickness and density of the fragment, respectively; $q(x,y)$ is the external load per unit area applied to the fragment at (x,y). $D = Eh^3/12(1-v^2)$, the bending stiffness of the plate, where E and v stand for the complex modulus of elasticity and Poisson's ratio of the material, respectively. Provided the fragment has a free

surface ($q(x,y)=0$), Eq. (2) becomes

$$\left[-\frac{\partial^2}{\partial x^2}M_x(x,y)-2\frac{\partial^2}{\partial x\partial y}M_{xy}(x,y)-\frac{\partial^2}{\partial y^2}M_y(x,y)\right]-\rho h\,\omega^2 w(x,y)=0 \tag{4}$$

Note that, although the isolated fragment described by Eq. (4) is free of external force, the internal forces and moments exerted by its adjacent fragments of the plate are still present on their sharing boundaries.

Now extend the above derivation to the entire plate containing a damaged zone (Θ) in Fig. 1(a). Without loss of the generality, Θ takes an arbitrary geometry. Then define

$$D=D_c[1-H(x,y)], \tag{5a}$$

$$\rho h=\rho_c h_c[1-G(x,y)], \tag{5b}$$

where

$$H(x,y)=\begin{cases}0 & (x,y)\notin\Theta\\ \alpha & (x,y)\in\Theta\end{cases}\ \text{and}\ G(x,y)=\begin{cases}0 & (x,y)\notin\Theta\\ \beta & (x,y)\in\Theta.\end{cases} \tag{6}$$

Here $H(x,y)$ and $G(x,y)$ are two two-dimensional Heaviside functions, each of which holds a non-zero constant within Θ but is zero outside Θ. D_c and $p_c h_c$ are the bending stiffness and the product of density and thickness of the plate component, respectively (both are for the intact region of the component); α and β ($0\le\alpha\le 1$ and $0\le\beta\le 1$) are the relative reductions in D_c and $\rho_c h_c$ within Θ with regard to those in the intact region, respectively. The attributes of Heaviside functions appropriately reflect the discontinuity at boundary of Θ, introducing perturbation to Eq. (4).

Substituting Eqs. (3) and (5) into Eq. (4) gives rise to, for the entire plate,

$$\begin{aligned}&\left\{\frac{\partial^2}{\partial x^2}\left\{D_c[1-H(x,y)]\left(\frac{\partial^2 w(x,y)}{\partial x^2}+\nu\frac{\partial^2 w(x,y)}{\partial y^2}\right)\right\}\right.\\&\quad+2\frac{\partial^2}{\partial x\partial y}\left\{D_c[1-H(x,y)](1-\nu)\frac{\partial^2 w(x,y)}{\partial x\partial y}\right\}\\&\left.\quad+\frac{\partial^2}{\partial y^2}\left\{D_c[1-H(x,y)]\left(\frac{\partial^2 w(x,y)}{\partial y^2}+\nu\frac{\partial^2 w(x,y)}{\partial x^2}\right)\right\}\right\}\\&\quad-\rho_c h_c[1-G(x,y)]\omega^2 w(x,y)=0.\end{aligned} \tag{7a}$$

With Eqs. (5) and (6), Eq. (7a) can further be expanded according to the differential rule, as

$$\begin{aligned}&-H''_{xx}D_c\left(\frac{\partial^2 w(x,y)}{\partial x^2}+\nu\frac{\partial^2 w(x,y)}{\partial y^2}\right)-2H''_{xy}D_c(1-\nu)\frac{\partial^2 w(x,y)}{\partial x\partial y}\\&\quad-H''_{yy}D_c\left(\frac{\partial^2 w(x,y)}{\partial y^2}+\nu\frac{\partial^2 w(x,y)}{\partial x^2}\right)\\&-2H'_xD_c\frac{\partial}{\partial x}\left(\frac{\partial^2 w(x,y)}{\partial x^2}+\nu\frac{\partial^2 w(x,y)}{\partial y^2}\right)-2H'_xD_c(1-\nu)\frac{\partial}{\partial y}\frac{\partial^2 w(x,y)}{\partial x\partial y}\\&-2H'_yD_c\frac{\partial}{\partial y}\left(\frac{\partial^2 w(x,y)}{\partial y^2}+\nu\frac{\partial^2 w(x,y)}{\partial x^2}\right)-2H'_yD_c(1-\nu)\frac{\partial}{\partial x}\frac{\partial^2 w(x,y)}{\partial x\partial y}\\&-HD_c\frac{\partial^2}{\partial x^2}\left(\frac{\partial^2 w(x,y)}{\partial x^2}+\nu\frac{\partial^2 w(x,y)}{\partial y^2}\right)-2HD_c(1-\nu)\frac{\partial^2}{\partial x\partial y}\frac{\partial^2 w(x,y)}{\partial x\partial y}\\&\quad-HD_c\frac{\partial^2}{\partial y^2}\left(\frac{\partial^2 w(x,y)}{\partial y^2}+\nu\frac{\partial^2 w(x,y)}{\partial x^2}\right)\\&+D_c\left(\frac{\partial^4 w(x,y)}{\partial x^4}+\nu\frac{\partial^4 w(x,y)}{\partial x^2\partial y^2}\right)+D_c\left(\frac{\partial^4 w(x,y)}{\partial y^4}+\nu\frac{\partial^4 w(x,y)}{\partial x^2\partial y^2}\right)\\&\quad+2D_c(1-\nu)\frac{\partial^2}{\partial x\partial y}\frac{\partial^2 w(x,y)}{\partial x\partial y}\\&\quad-\rho_c h_c[1-G(x,y)]\omega^2 w(x,y)=0.\end{aligned} \tag{7b}$$

In Eq. (7b), H is the abbreviation of $H(x,y)$; $H'_x=(\partial/\partial x)H(x,y)$, $H'_y=(\partial/\partial y)H(x,y)$, $H''_{xx}=(\partial^2/\partial x^2)H(x,y)$, $H''_{yy}=(\partial^2/\partial y^2)H(x,y)$ and $H''_{xy}=(\partial^2/\partial x\partial y)H(x,y)$. Because H is either a non-zero constant within Θ or zero outside of Θ, it is anticipated that the derivatives of H (H'_x, H'_y, H''_{xx}, H''_{yy} and H''_{xy}) are zero across the entire plate except at the boundary of Θ where singularity is

present, leading to prominent peaks (associated with H'_x and H'_y) and drastic oscillations (associated with H''_{xx}, H''_{yy} and H''_{xy}) at the boundary of Θ.

Furthermore, substituting Eqs. (3) into (7b) yields

$$\begin{aligned}
&H''_{xx}M_x(x,y)+2H''_{xy}M_{xy}(x,y)+H''_{yy}M_y(x,y)\\
&+2H'_x\left(\frac{\partial}{\partial x}M_x(x,y)+\frac{\partial}{\partial y}M_{xy}(x,y)\right)+2H'_y\left(\frac{\partial}{\partial y}M_y(x,y)+\frac{\partial}{\partial x}M_{xy}(x,y)\right)\\
&-HD_c\left(\frac{\partial^4 w(x,y)}{\partial x^4}+2\frac{\partial^4 w(x,y)}{\partial x^2\partial y^2}+\frac{\partial^4 w(x,y)}{\partial y^4}\right)\\
&+D_c\left(\frac{\partial^4 w(x,y)}{\partial x^4}+2\frac{\partial^4 w(x,y)}{\partial x^2\partial y^2}+\frac{\partial^4 w(x,y)}{\partial y^4}\right)\\
&-\rho_c h_c\omega^2 w(x,y)+\rho_c h_c G(x,y)\omega^2 w(x,y)=0.
\end{aligned} \tag{8}$$

On the other hand, according to the local equilibrium of a plate component [27], one has

$$Q_x(x,y)=\frac{\partial M_x(x,y)}{\partial x}+\frac{\partial M_{yx}(x,y)}{\partial y}, \tag{9a}$$

$$Q_y(x,y)=\frac{\partial M_y(x,y)}{\partial y}+\frac{\partial M_{xy}(x,y)}{\partial x}, \tag{9b}$$

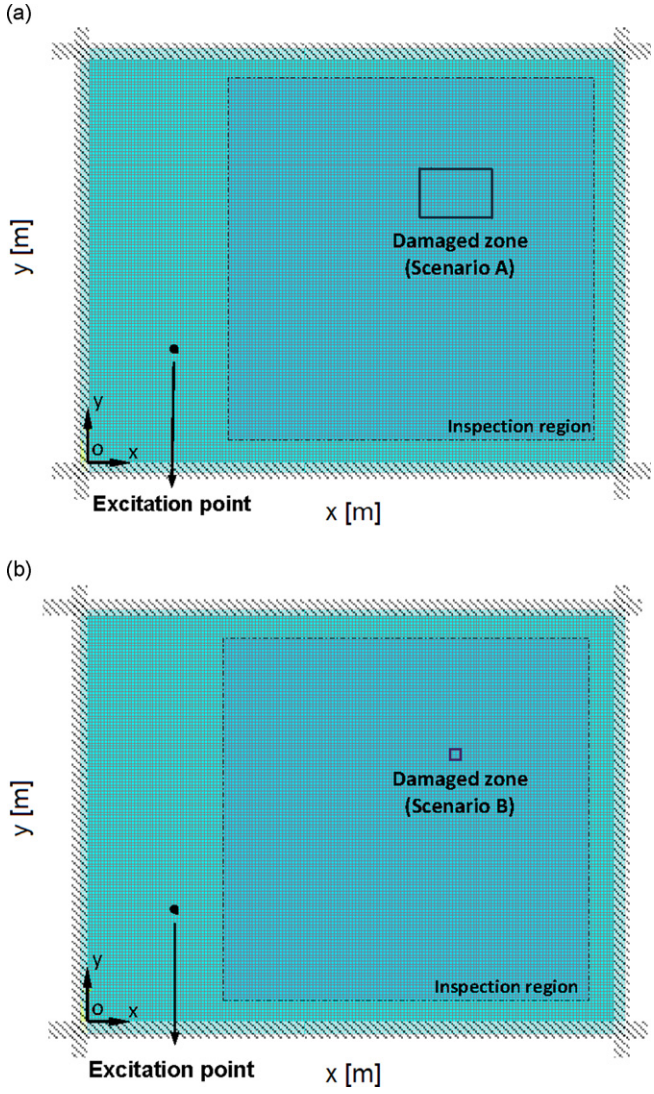

Fig. 2. FE models for damage scenarios (a) A and (b) B used in proof-of-concept validation.

where $Q_x(x,y)$ and $Q_y(x,y)$ are the shear forces along x- and y-axes, respectively, as indicated in Fig. 1(b), exerted by adjacent fragments of the plate. With them, Eq. (8) can be rearranged as

$$D_c\left(\frac{\partial^4 w(x,y)}{\partial x^4}+2\frac{\partial^4 w(x,y)}{\partial x^2\partial y^2}+\frac{\partial^4 w(x,y)}{\partial y^4}\right)-\rho_c h_c\omega^2 w(x,y)$$
$$=\left\{-H''_{xx}M_x(x,y)-2H''_{xy}M_{xy}(x,y)-H''_{yy}M_y(x,y)-2H'_xQ_x(x,y)-2H'_yQ_y(x,y)\right\}$$
$$+\left\{HD_c\left(\frac{\partial^4 w(x,y)}{\partial x^4}+2\frac{\partial^4 w(x,y)}{\partial x^2\partial y^2}+\frac{\partial^4 w(x,y)}{\partial y^4}\right)-\rho_c h_c G(x,y)\omega^2 w(x,y)\right\}. \quad (10)$$

The left-hand side of Eq. (10) is namely the damage index (DI) for the entire plate, a two-dimensional index, defined as

$$\mathrm{DI}=D_c\left(\frac{\partial^4 w(x,y)}{\partial x^4}+2\frac{\partial^4 w(x,y)}{\partial x^2\partial y^2}+\frac{\partial^4 w(x,y)}{\partial y^4}\right)-\rho_c h_c\omega^2 w(x,y). \quad (11)$$

It is noteworthy that Eq. (11), a localized equilibrium equation, applies to every single point of the plate including both the intact and damaged zones. It depicts local equilibrium between the inertia forces of a plate fragment and the forces/moments exerted by its adjacent elements. For an explicit expression, DI is split as follows in terms of Eq. (6),

$$\mathrm{DI}=0,\ ((x,y)\notin\Theta) \quad (12a)$$

$$\mathrm{DI}=-H''_{xx}M_x(x,y)-2H''_{xy}M_{xy}(x,y)-H''_{yy}M_y(x,y)$$
$$-2H'_xQ_x(x,y)-2H'_yQ_y(x,y)\quad(\text{at boundary of }\Theta) \quad (12b)$$

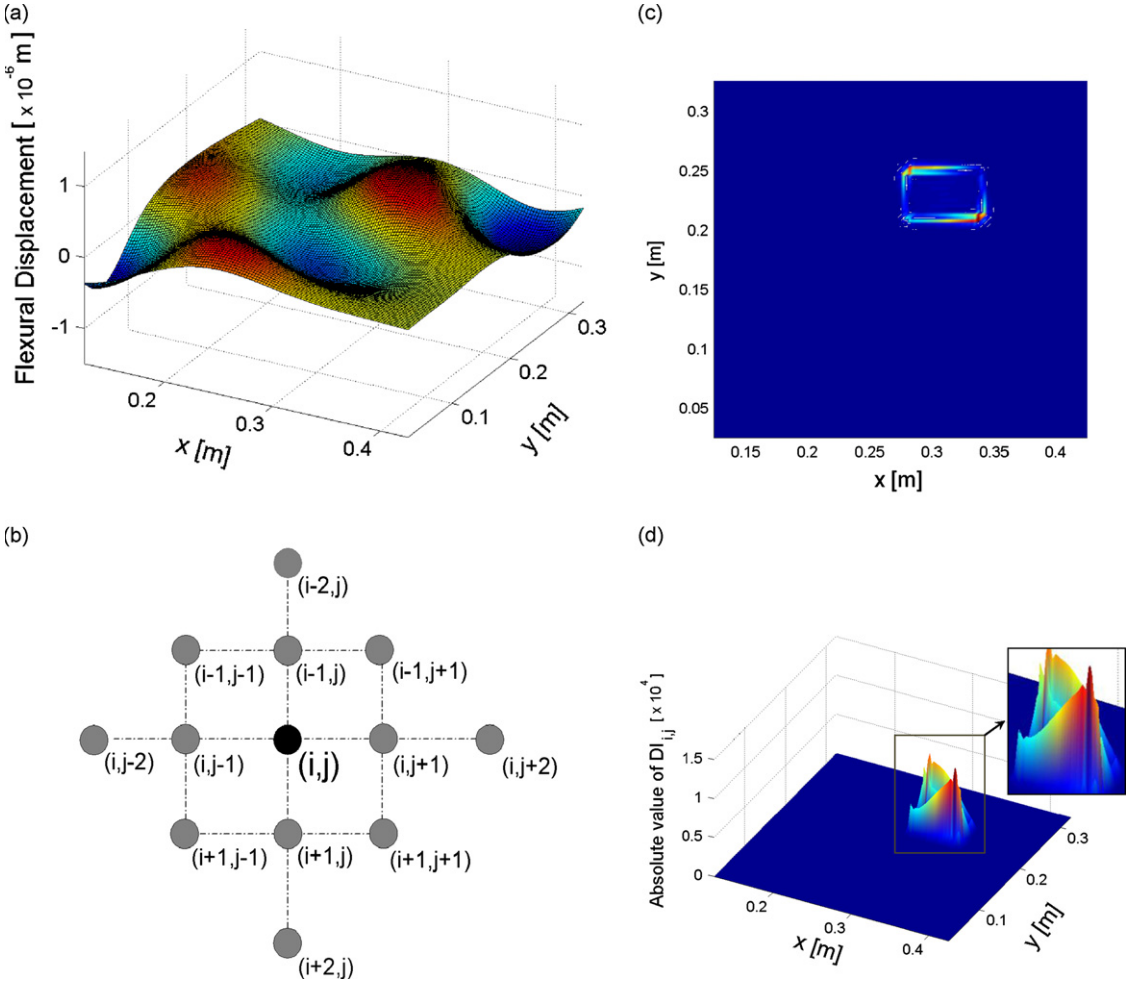

Fig. 3. (a) Flexural vibration displacement ($w_{i,j}$) of the damaged plate in scenario A at 1100 Hz ($\lambda=0.16$ m); (b) schematic of measurement points involved in two-dimensional finite difference calculation for target point (i,j); and accordingly constructed $\mathrm{DI}_{i,j}$ over inspection region in (c) two- and (d) three-dimensional presentations.

$$\mathrm{DI} = \alpha D_c \left(\frac{\partial^4 w(x,y)}{\partial x^4} + 2\frac{\partial^4 w(x,y)}{\partial x^2 \partial y^2} + \frac{\partial^4 w(x,y)}{\partial y^4} \right) - \beta \rho_c h_c \omega^2 w(x,y) \quad ((x,y) \in \Theta) \tag{12c}$$

Inherently, distribution of DI over the plate presents explicit physical meanings:

(1) in the intact region (defined by Eq. (12a)), DI is, in principle, zero, although it may not be the case in practice due to measurement noise and uncertainties (to be discussed in subsequent sections);
(2) along boundary of Θ (defined by Eq. (12b)), DI exhibits certain fluctuation with a magnitude subjected to damage-induced shear forces ($Q_x(x,y)$ and $Q_y(x,y)$), bending ($M_x(x,y)$ and $M_y(x,y)$) and torsion moments ($M_{xy}(x,y)$) along the boundary. This is a preferable feature to depict the damaged zone; and
(3) within Θ (defined by Eq. (12c)), DI smoothly varies with a magnitude subjected to α and β, provided the material and geometry are still continuous within Θ (but they are different from those outside of Θ).

Eq. (12) alludes to that the vibration of a plate-like component bearing a damaged zone can be equivalent to that of its pristine counterpart subject to concentrated '*external*' shear forces, bending and torsion moments applied along the boundaries of the damaged zone. These '*external*' forces and moments are actually due to the singularities arising from the discontinuity in the material and geometry (due to damage presence), which are exerted by adjacent fragments of the plate, instead of true external forces. Thus, they are called *pseudo-forces* and *pseudo-moments* incurred by the damage in this study. According to Eq. (12), DI can be developed using the material and geometric parameters of the intact region; any drastic oscillation in DI, if perceived, indicates existence of damage therein; and its distribution can further facilitate quantitative characterization of the damage.

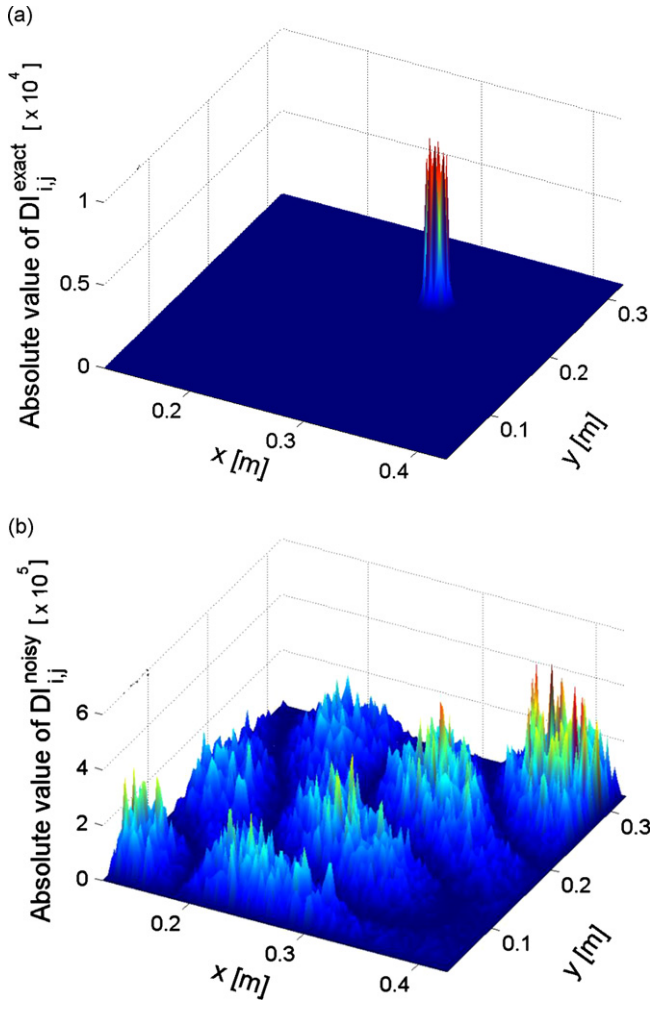

Fig. 4. Constructed $\mathrm{DI}_{i,j}$ over inspection region of the damaged plate in scenario B at 1100 Hz ($\lambda = 0.16$ m) using (a) noise-free and (b) noise-contaminated nodal displacements.

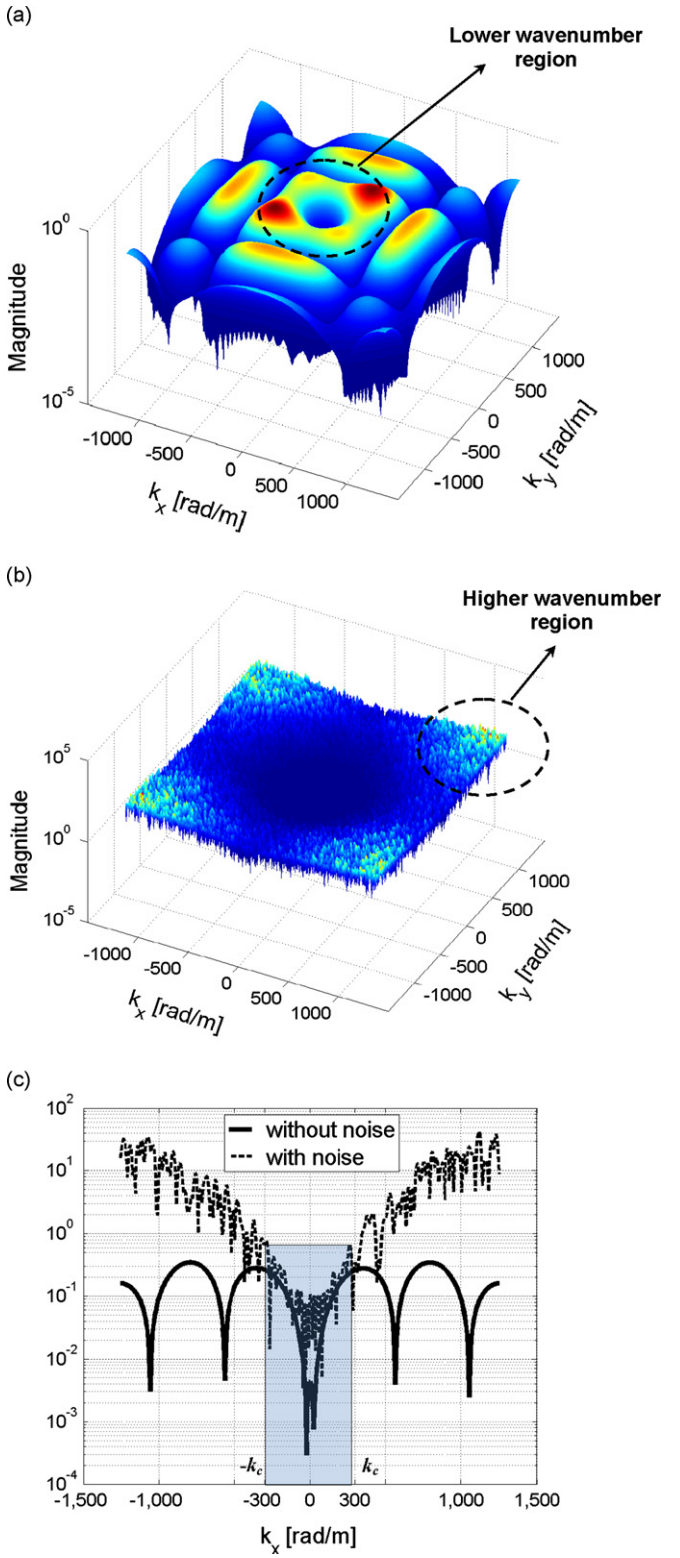

Fig. 5. Two-dimensional FFT spectra of (a) $DI_{i,j}^{exact}$ and (b) $DI_{i,j}^{noisy}$ for the damaged plate in scenario B; and (c) combined presentation of (a) and (b) by setting $k_y = 0$.

It is relevant to note that the above derivation is based on the Kirchhoff–Love hypothesis, requiring the uniformity of the material and geometric properties, as well as the de-coupling between the in-plane and out-of-plane motion of the discussed plate. For more general scenarios in which the material properties are not uniform or the thickness of the plate component varies, the rationale of DI development is still tenable, provided that the motion of the plate component under investigation can be mathematically modeled.

In practical manipulation, DI (Eq. (12)) can be constructed using a finite difference method as follows. The inspection region is first discretized using $N \times M$ measurement points, and for each point (i,j) $(i=1,2,\ldots,N;\ j=1,2,\ldots,M)$, DI is calculated in accordance with

$$\mathrm{DI}_{i,j} = D_c(\chi_{i,j}^{4x} + 2\chi_{i,j}^{2x2y} + \chi_{i,j}^{4y}) + ph_c\omega^2 w_{i,j} \tag{13}$$

In the above, $w_{i,j}$ is the flexural displacement of the plate measured at (i,j), and

$$\chi_{i,j}^{4x} = \frac{\partial^4 w}{\partial x^4} = \frac{1}{\Delta_x^4}(w_{i+2,j} - 4w_{i+1,j} + 6w_{i,j} - 4w_{i-1,j} + w_{i-2,j}) \tag{14a}$$

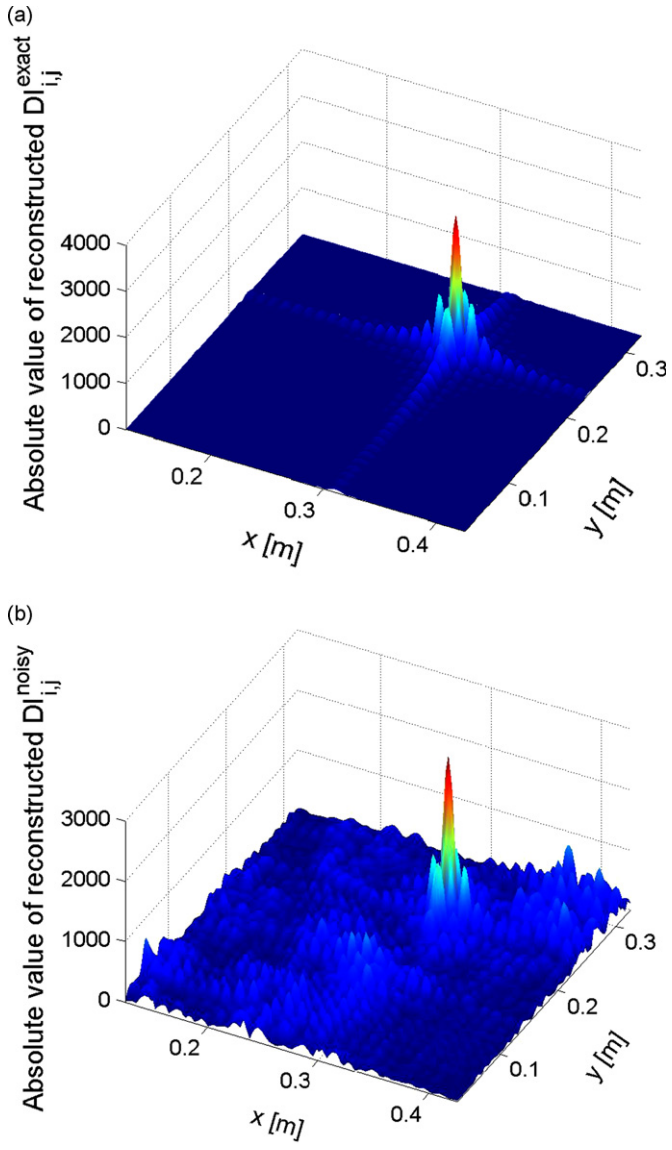

Fig. 6. Re-constructed (a) $\mathrm{DI}_{i,j}^{\mathrm{exact}}$; and (b) $\mathrm{DI}_{i,j}^{\mathrm{noisy}}$ for the damaged plate in scenario B via inverse two-dimensional FFT ($k_c = 300$ rad/m).

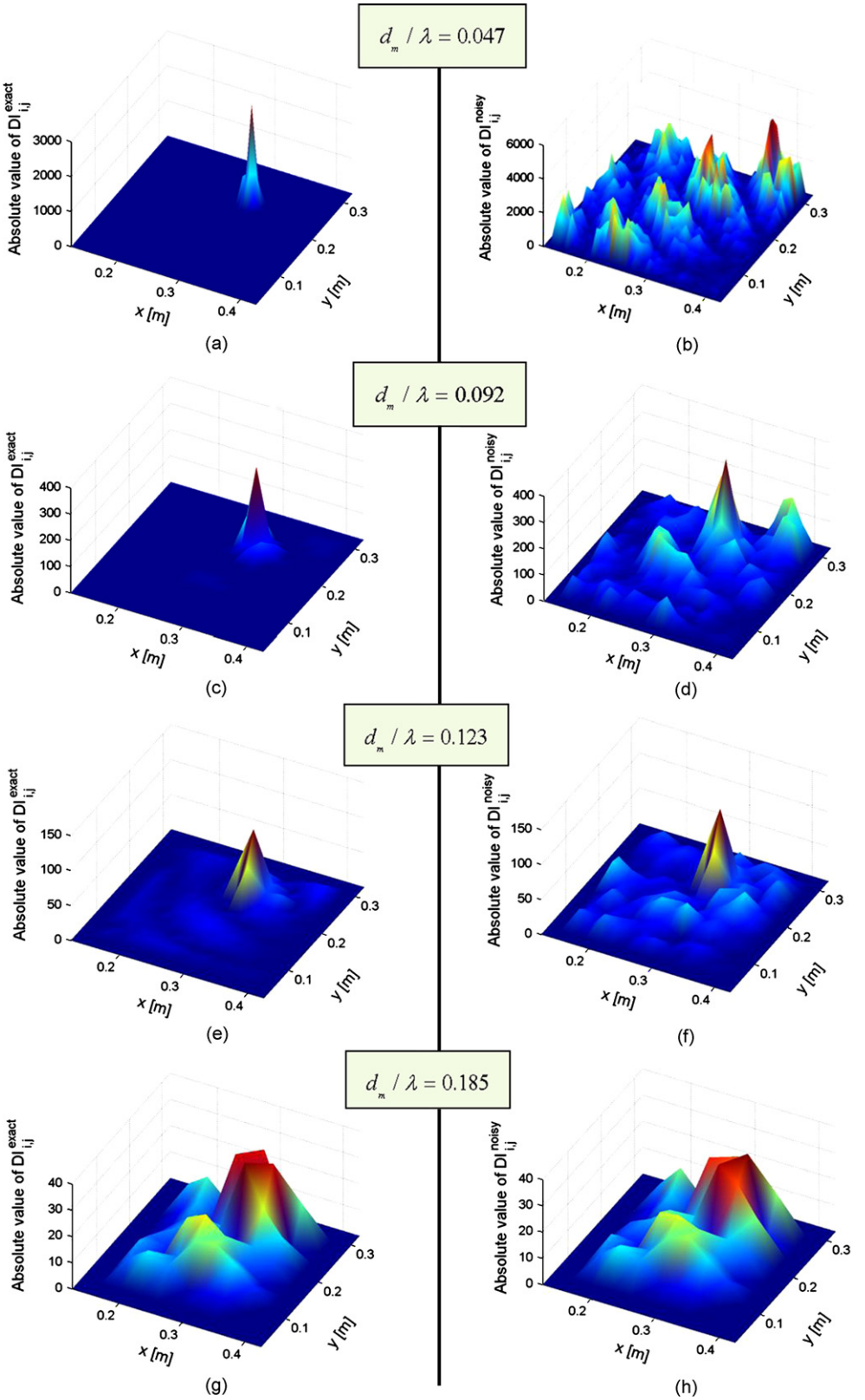

Fig. 7. Constructed $DI^{exact}_{i,j}$ (left column) and $DI^{noisy}_{i,j}$ (right column) for the damaged plate in scenario B when d_m/λ is (a) and (b) 0.047; (c) and (d) 0.092; (e) and (f) 0.123; (g) and (h) 0.185.

$$\chi_{i,j}^{4y} = \frac{\partial^4 w}{\partial y^4} = \frac{1}{\Delta_y^4}(w_{i,j+2} - 4w_{i,j+1} + 6w_{i,j} - 4w_{i,j-1} + w_{i,j-2}) \tag{14b}$$

$$\chi_{i,j}^{2x2y} = \frac{\partial^4 w}{\partial^2 x \partial^2 y} = \frac{1}{\Delta_x^2 \Delta_y^2}(w_{i+1,j+1} - 2w_{i+1,j} + w_{i+1,j-1} - 2w_{i,j+1} + 4w_{i,j} - 2w_{i,j-1} + w_{i-1,j+1} - 2w_{i-1,j} + w_{i-1,j-1}), \tag{14c}$$

where Δ_x and Δ_y are the intervals between two adjacent measurement points along the x- and y-axes, respectively. Note that determination of the number of measurement points for the above finite difference calculation is to be discussed in Section 3.3.2. It is also relevant to know that to construct DI across the whole inspection region, the vibration responses in the inspection region boundary must be captured, which may lead to erroneous results therein due to insufficient measurement points.

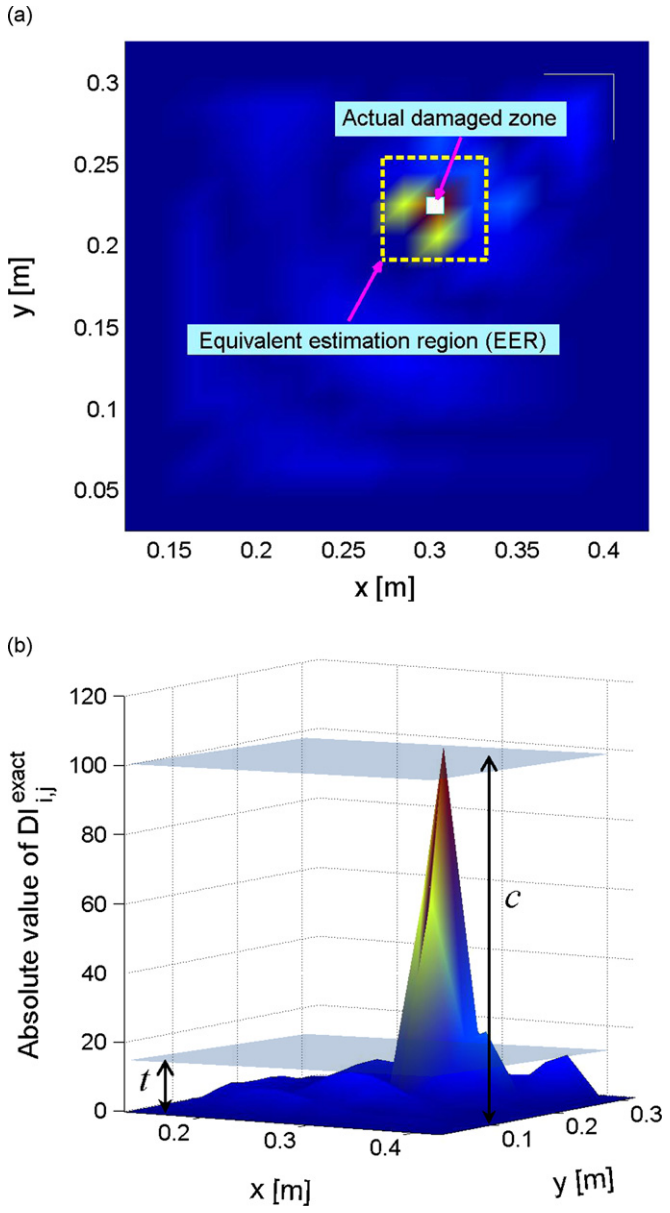

Fig. 8. Illustration for definition of (a) equivalent estimation region (EER) and (b) AD.

3. Proof-of-concept validation using numerical simulation

Feasibility of using the developed two-dimensional damage index to characterize damage in plate components was first examined through finite element (FE) simulation. A rectangular aluminum plate ($450 \times 350 \times 3$ mm^3; density: 2.7 kg/m^3; Young's modulus: $70 \times (1+10^{-3}i)$ GPa), simply supported at its four edges was considered, as shown in Fig. 2. The effect of material damping was comprehended in the complex modulus of elasticity. A point-force source was applied to generate harmonic excitation perpendicular to the plate with an arbitrarily selected frequency of 1100 Hz. To eliminate possible singularity near the force source, an inspection region (300×300 mm^2) was defined (highlighted in Fig. 2), excluding the vicinity of the source.

Two damage cases (scenarios A and B), in Fig. 2(a) and (b), respectively, were hypothesized: in scenario A, the plate contained a relatively large damaged zone centered at (310, 230) (measuring 60×40 mm^2, accounting for ca. 1.5% of the overall area of the plate); in B, the plate had a relatively small damaged zone centered at the same location (10×10 mm^2, being approximately 0.06% of the overall area of the plate). The former was aimed at comprehending the distribution characteristics of DI, while the latter at gauging the capacity of *DI* in characterizing damage small in size. For both scenarios, the damage was simulated by a reduction in the thickness by one-third of that in the intact region. Two damaged plates were uniformly meshed using three-dimensional brick elements, $5 \times 5 \times 1$ mm^3 each, with three layers across the plate thickness. The flexural displacements, $w_{i,j}$, at all FE nodes (an FE node is corresponding to a measurement point in experiment) on the intact plate surface, opposite to which lay the damaged zone, was obtained using the commercial FE code ANSYS®.

3.1. Construction of damage index (ideal case without measurement noise)

For scenario A, the calculated $w_{i,j}$ over inspection region is shown in Fig. 3(a), from which no straightforward information associated with the damage can be captured. To construct $\mathrm{DI}_{i,j}$ using Eq. (13), thirteen points were selected for finite difference calculation, as illustrated in Fig. 3(b), where a uniform difference interval, d_m, along x- and y-axes was adopted (*i.e.*, $\Delta_x = \Delta_y = d_m$). The accordingly constructed $\mathrm{DI}_{i,j}$ across inspection region was two- and three-dimensionally presented in Fig. 3(c) and (d), respectively. It can be seen that $\mathrm{DI}_{i,j}$ remains null in the intact region of the plate, but drastically deviates from zero at the boundary of the damaged zone. The evidenced boundary is able to accurately depict the location, shape and even rough size of the damaged zone. It is noteworthy that $\mathrm{DI}_{i,j}$ varies along each edge of the damaged zone, clearly reflected in the insert of Fig. 3(d). Such a variation can be attributed to the dependence of $\mathrm{DI}_{i,j}$ on $M_x(x,y)$, $M_y(x,y)$, $M_{xy}(x,y)$, $Q_x(x,y)$ and $Q_y(x,y)$ according to Eq. (12), which are distinct at different spatial locations of the plate. Processed in a same fashion, the constructed $\mathrm{DI}_{i,j}$ for scenario B is exhibited in Fig. 4(a). Down to such a tiny scale, individual edges of this small damaged zone are not isolated clearly, but it suffices to signal the existence, location, shape and overall size of the damaged zone.

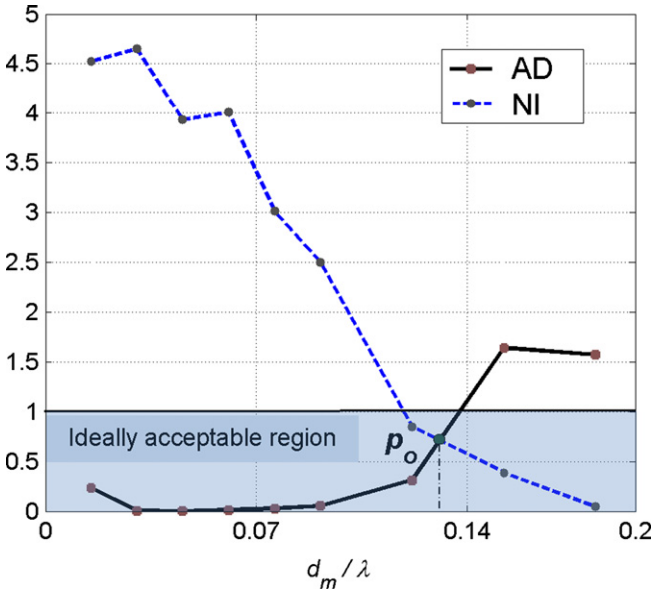

Fig. 9. Variation in AD and NI for the damaged plate in scenario B at different d_m/λ ($r_c = 0.4$, $\Xi_c = 0.8$).

3.2. Construction of damage index (realistic case with measurement noise)

It is however envisaged that the captured $w_{i,j}$ can be prone to the contamination from measurement noise and uncertainties, boundary effects and error of finite difference calculation, potentially dimming those damage-associated features in $w_{i,j}$ and leading to compromised or even erroneous identification. Moreover, it is foreseen that $\mathrm{DI}_{i,j}$ in Eq. (12) can be fairly susceptible to noise interference, because the noise in $w_{i,j}$ can become dominant upon fourth-order differentiation (*e.g.*, $\partial^4 w(x,y)/\partial x^4$). It is thus of vital necessity to gauge the tolerance of the proposed damage index to measurement noise. To this end, the calculated nodal flexural displacement was numerically polluted by

$$w_{i,j}^{\mathrm{noisy}} = w_{i,j}^{\mathrm{exact}}\varepsilon_p + \varepsilon_b, \tag{15}$$

where

$$\varepsilon_p = \Delta w e^{j\Delta\varphi} \text{ and } \varepsilon_b = \varepsilon_b^R + j\varepsilon_b^i$$

In the above, $w_{i,j}^{\mathrm{exact}}$ and $w_{i,j}^{\mathrm{noisy}}$ are the flexural displacement at (i,j) in the absence of noise and its corresponding noise-polluted counterpart, respectively; the measurement error, ε_p, is proportional to $w_{i,j}^{\mathrm{exact}}$ (where Δw and $\Delta\varphi$ are two Gaussian random real numbers related to the magnitude and phase of $w_{i,j}^{\mathrm{exact}}$, respectively); ε_b, the background noise, is constituted by ε_b^R and ε_b^I (another two Gaussian random real numbers associated with the real and imaginary parts of $w_{i,j}^{\mathrm{exact}}$, respectively, subject to measurement equipment).

For comparative discussion, assuming that (i) the average of Δw is one, and the averages of $\Delta\varphi$, ε_b^R and ε_b^I are zero, and (ii) their corresponding standard derivations are: $\sigma\{\Delta w\} = 1\%$, $\sigma\{\Delta\sigma\} = 1^\circ$ and $\sigma\{\varepsilon_b^R\} = \sigma\{\varepsilon_b^I\} = 10^{-10}$ m; and (iii) all other parameters in simulation remain unchanged, then the constructed damage index for scenario B using $w_{i,j}^{\mathrm{noisy}}$ (denoted by

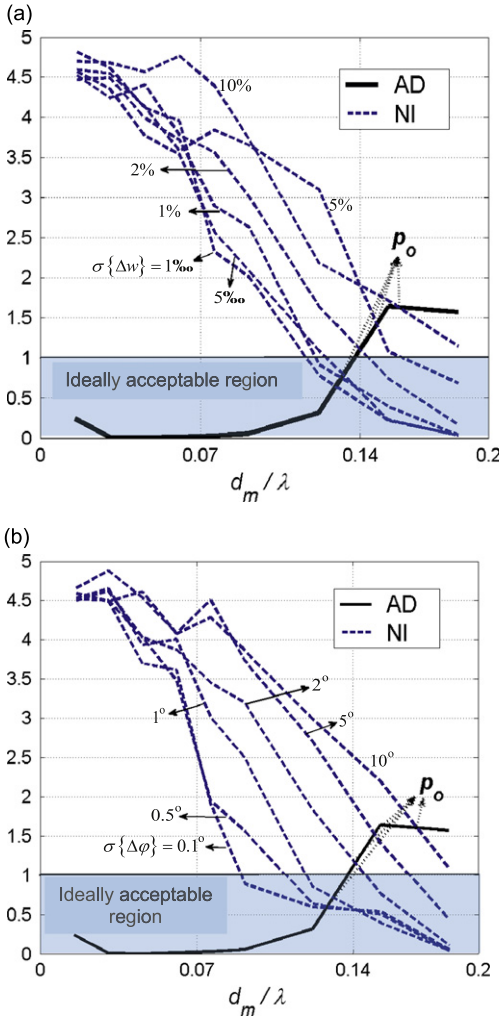

Fig. 10. Variation in AD–NI curves for the damaged plate in scenario B subject to different levels of measurement noise in (a) magnitude and (b) phase ($r_c = 0.4$, $\Xi_c = 0.8$).

$DI_{i,j}^{noisy}$ hereinafter) is shown in Fig. 4(b). It can be seen that under the noise interference, recognition of signal features pertaining to damage becomes intractable, because the measurement noise, even tiny (1% in this example), is considerably boosted upon the fourth-order differentiation.

3.3. De-noising Techniques

The connatural vulnerability of the proposed damage index to measurement noise entailed de-noising treatment. Two independent de-noising techniques were developed: *Low-pass Wavenumber Filtering* (LWF) and *Adjustment of Measurement Density* (AMD).

3.3.1. LWF

LWF is a post-processing initiative based on spectrum analysis, motivated by the observation that the signal features relating to random noise and to the damage are clustered in different regions in the wavenumber domain [1]. By way of illustration, Fig. 5 shows the spectra of $DI_{i,j}^{exact}$ (Fig. 4(a)) and $DI_{i,j}^{noisy}$ (Fig. 4(b)) obtained using the two-dimensional Fast Fourier Transform (FFT), to notice that the majority of wavenumbers of $DI_{i,j}^{exact}$ are concentrated in a relatively lower wavenumber region (Fig. 5(a)), whereas the noise influence plays a dominant role in a relatively higher wavenumber region (Fig. 5(b)). For further comparison, two-dimensional FFT results of $DI_{i,j}^{exact}$ and $DI_{i,j}^{noisy}$ by setting $k_y = 0$ were combined in Fig. 5(c), manifesting an overlap between two indices only in a certain range ($-k_c < k_x < k_c$, where k_x is the wavenumber along x-axis). Because of the isotropic material properties of the plate, a similar overlap at $-k_c < k_y < k_c$ (by setting $k_x = 0$, where k_y the wavenumber along y-axis) is foreseen. Based on this, an LWF function was designed to screen out noise interference at the higher wavenumber region while maintaining signal features in the lower region, which is

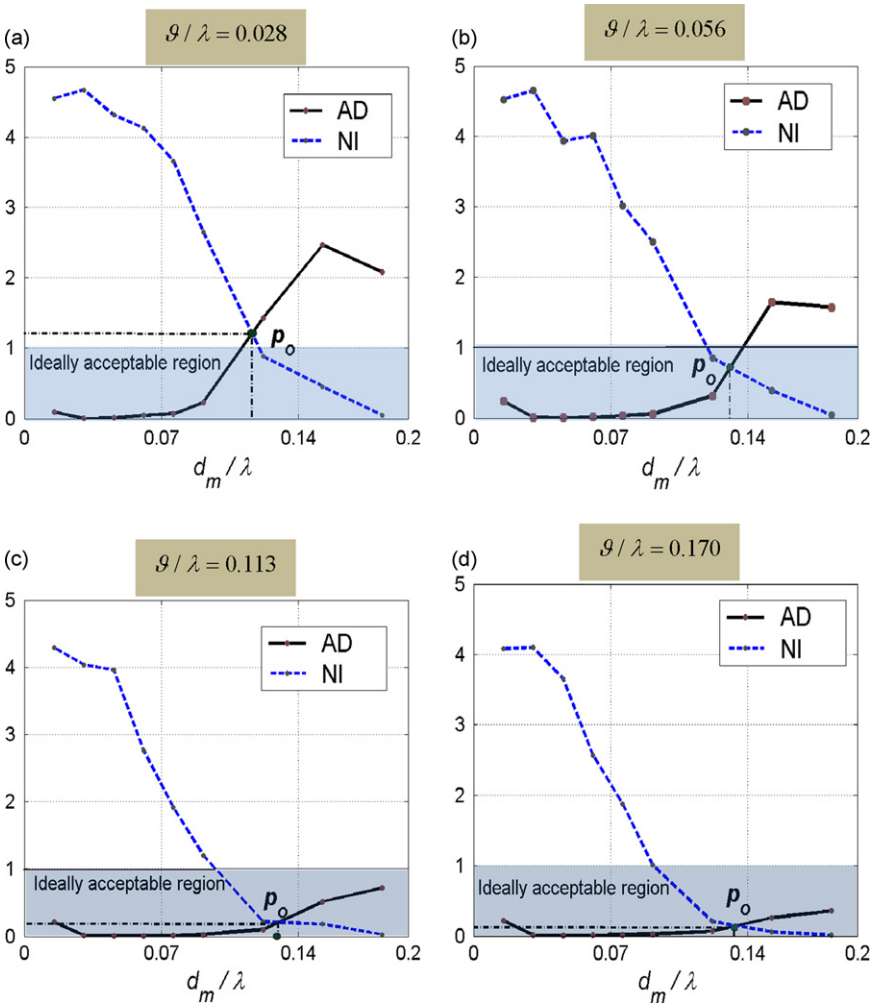

Fig. 11. Variation in AD–NI curves for the damaged plate in scenario B when ϑ/λ is (a) 0.028; (b) 0.056; (c) 0.113; and (d) 0.170 (thickness reduction: 0.33, $r_c = 0.4$, $\Xi_c = 0.8$).

defined as

$$\tilde{h}(k_x,k_y)=\begin{cases}1 & \text{when } (|k_x| \le k_c \text{ and } |k_y| \le k_c)\\ 0 & \text{otherwise}\end{cases} \tag{16}$$

where $\tilde{h}(k_x,k_y)$ is a filtering function, and k_c the cutoff wavenumber with a unit of rad m^{-1}. Similar to a Heaviside function, Eq. (16) eliminates signal features outside of the range in which $DI_{i,j}^{exact}$ and $DI_{i,j}^{noisy}$ overlap in the wavenumber spectrum. Upon application of LWF, the residual signal features can be re-constructed back to the spatial domain using the inverse two-dimensional FFT. Furthermore, to avoid numerical errors near the fringe of the inspection region due to insufficient measurement points for finite difference calculation (known as the *Gibbs phenomenon* [28]), a two-dimensional *Hanning* window in the spatial domain was applied prior to LWF [1]. Subsequently applied with the *Hanning* window, LWF and inverse two-dimensional FFT, the re-constructed $DI_{i,j}^{exact}$ and $DI_{i,j}^{noisy}$ are displayed in Fig. 6(a) and (b), respectively, showing a substantially improved resolution compared with Fig. 4. Both highlight not only the location of the damaged zone but its approximate size, even under the interference of measurement noise (Fig. 6(b)).

3.3.2. AMD

Independent of LWF, AMD is an alternative to enhance the robustness of the proposed damage index in noisy measurement conditions, residing on a correlation between the degree of noise influence and the density of measurement points (*viz.*, the distance between two adjacent measurement points, d_m, *i.e.*, the differential interval Δ_x or Δ_y in Eq. (14)). It is anticipated that with an increase in d_m, the accuracy of finite difference calculation decreases as a result of the increasing truncation errors, and in the meanwhile the noise interference is alleviated, giving rise to enhanced noise

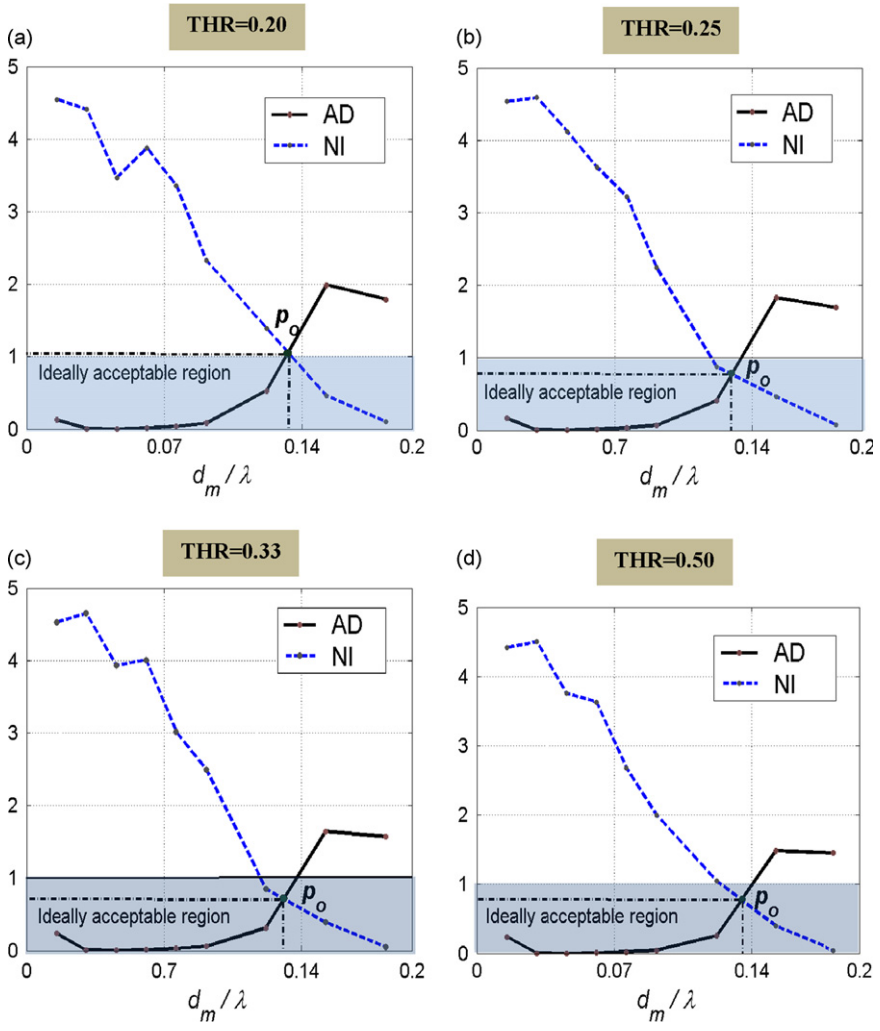

Fig. 12. Variation in AD–NI curves for the damaged plate in scenario B when THR is (a) 0.20; (b) 0.25; (c) 0.33; and (d) 0.50 ($\vartheta/\lambda=0.056$, $r_c=0.4$ and $\Xi_c=0.8$).

immunity, and vice versa. Thus, it is crucial to strike a balance between the accuracy of finite difference calculation and the noisy immunity of damage index, through optimizing d_m. Considering that the damage index makes use of harmonic vibration signals which exhibit periodical patterns in the spatial domain, a dimensionless parameter, d_m/λ, was established (λ: wavelength of the vibration of the plate at a given harmonic excitation).

For illustration, $DI_{i,j}^{exact}$ and $DI_{i,j}^{noisy}$ for damage scenario B (Fig. 2(b)), constructed at four exemplary d_m/λ ($d_m/\lambda = 0.047,\ 0.092,\ 0.123,\ 0.185$), are compared in Fig. 7. It can be seen that as d_m/λ increases, the damage identification accuracy reduces, implying that both $DI_{i,j}^{exact}$ and $DI_{i,j}^{noisy}$ progressively lose their capabilities of predicting damage. On the other hand, such a reduction in accuracy is accompanied with an enhanced immunity to measurement noise, evidenced by an increasing similarity between $DI_{i,j}^{exact}$ and $DI_{i,j}^{noisy}$. This observation alludes to a dual-effect of d_m/λ: using less measurement points (greater d_m/λ) can enhance the noise immunity of the damage index, but this is at the expense of sacrificing the accuracy of finite difference calculation, and vice versa. In particular, for the discussed case, the option in which $d_m/\lambda = 0.123$ (Fig. 7(e) and (f)) contributes to a reasonable balance, and with it the damage location can be identified directly from the distribution of $DI_{i,j}^{noisy}$ without any de-noising treatment such as LWF. This option of d_m/λ can therefore be deemed as an optimal configuration to match the current excitation. It is interesting to note that this selection ($d_m/\lambda = 0.123$) corresponds to roughly nine measurement points per wavelength.

To quantify the above dual-effect, two normalized signal parameters, AD (*Accuracy of finite Difference*) and NI (*Noise Influence*), were introduced.

3.3.2.1. Accuracy of Finite Difference (AD). For illuminating the nature of AD, use $DI_{i,j}^{exact}$ when $d_m/\lambda = 0.123$ (Fig. 7(e)) and define an *equivalent estimation region* (EER) as highlighted in Fig. 8(a). EER embraces all the peaks of $DI_{i,j}^{exact}$ at the boundary of damaged zone, and its size is in principle larger than the actual damaged zone because construction of $DI_{i,j}^{exact}$ at damage boundary involves neighboring measurement points beyond the damaged zone (subject to d_m). Letting the peak value of $DI_{i,j}^{exact}$ within and outside of EER be c and t, respectively, as illustrated in Fig. 8(b), and the ratio of t/c be r, then a dimensionless parameter AD is defined as

$$AD = \frac{r}{r_c} = \frac{t}{c\,r_c}, \tag{17}$$

where r_c is a threshold. The numerator r depicts the degree of protrusion of $DI_{i,j}^{exact}$ induced by damage in the damaged zone with regard to $DI_{i,j}^{exact}$ in intact region. Damage incurs variation in $DI_{i,j}^{exact}$, and accordingly AD has the capability of

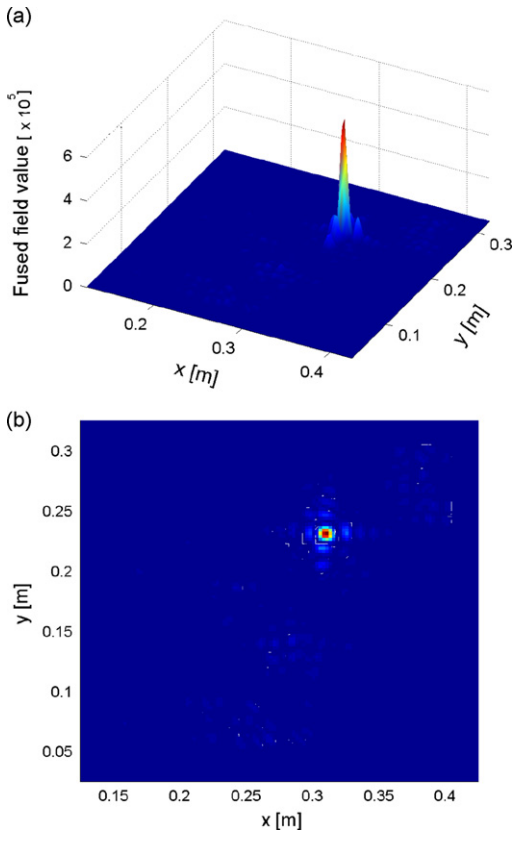

Fig. 13. (a) Two and (b) three-dimensional presentations of fused ultimate image for the damaged plate in scenario B.

reflecting the identification accuracy. Provided r is greater than r_c (*i.e.*, AD >1), the accuracy is deemed unacceptable, and vice versa. In other words, the accuracy is satisfactory only when AD falls in the range of [0,1]. In the following discussion, r_c was set to be 0.4, which has been demonstrated effective to judge the identification accuracy.

3.3.2.2. Noise influence (NI). NI, also a dimensionless index, is defined in the light of a quantitative resemblance between $\mathrm{DI}_{i,j}^{\mathrm{exact}}$ and $\mathrm{DI}_{i,j}^{\mathrm{noisy}}$ at a specific spatial location. The resemblance is calibrated using a two-dimensional correlation coefficient, Ξ, given by

$$\Xi=\frac{N\sum_{i=1}^{N_y}\sum_{j=1}^{N_x}\mathrm{DI}_{i,j}^{\mathrm{exact}}\mathrm{DI}_{i,j}^{\mathrm{noisy}}-\sum_{i=1}^{N_y}\sum_{j=1}^{N_x}\mathrm{DI}_{i,j}^{\mathrm{exact}}\sum_{i=1}^{N_y}\sum_{j=1}^{N_x}\mathrm{DI}_{i,j}^{\mathrm{noisy}}}{\sqrt{N\sum_{i=1}^{N_y}\sum_{j=1}^{N_x}\left(\mathrm{DI}_{i,j}^{\mathrm{exact}}\right)^2-\left(\sum_{i=1}^{N_y}\sum_{j=1}^{N_x}\mathrm{DI}_{i,j}^{\mathrm{exact}}\right)^2}\sqrt{N\sum_{i=1}^{N_y}\sum_{j=1}^{N_x}\left(\mathrm{DI}_{i,j}^{\mathrm{noisy}}\right)^2-\left(\sum_{i=1}^{N_y}\sum_{j=1}^{N_x}\mathrm{DI}_{i,j}^{\mathrm{noisy}}\right)^2}}, \tag{18}$$

where N_x and N_y are the numbers of measurement points along x- and y-axes within the inspection region, respectively. Theoretically, Ξ varies in the range of [0,1], and in particular the unity of Ξ ($\Xi=1$) indicates a perfect matching between $\mathrm{DI}_{i,j}^{\mathrm{exact}}$ and $\mathrm{DI}_{i,j}^{\mathrm{noisy}}$ (*i.e.*, the ideal case without noise influence). Similar to the way of defining AD, a threshold, Ξ_c, is introduced to evaluate the acceptability of noise influence, with which NI is defined as

$$\mathrm{NI}=\frac{1-\Xi}{1-\Xi_c} \tag{19}$$

Provided Ξ is less than Ξ_c (*i.e.*, NI >1, indicating a low similarity between $\mathrm{DI}_{i,j}^{\mathrm{exact}}$ and $\mathrm{DI}_{i,j}^{\mathrm{noisy}}$), the influence of noise is considered unacceptable, leading to poor recognizability of signals and making identification impossible without proper de-noising treatment. Similar as AD, an acceptable NI should fall in the range of [0, 1]. Ξ_c was set to be 0.8 hereinafter, demonstrated sufficient to screen noise influence.

Simultaneous consideration of AD and NI via Eqs. (17) and (19) provides a straightforward means to balance the accuracy of finite difference calculation with noise immunity. Ideally, both AD and NI should concurrently fall in the range of [0, 1], and such a range is called '*ideally acceptable region*' in what follows, in which $0<\mathrm{AD}\le 1$ and $0<\mathrm{NI}\le 1$. For illustration, Fig. 9 shows AD and

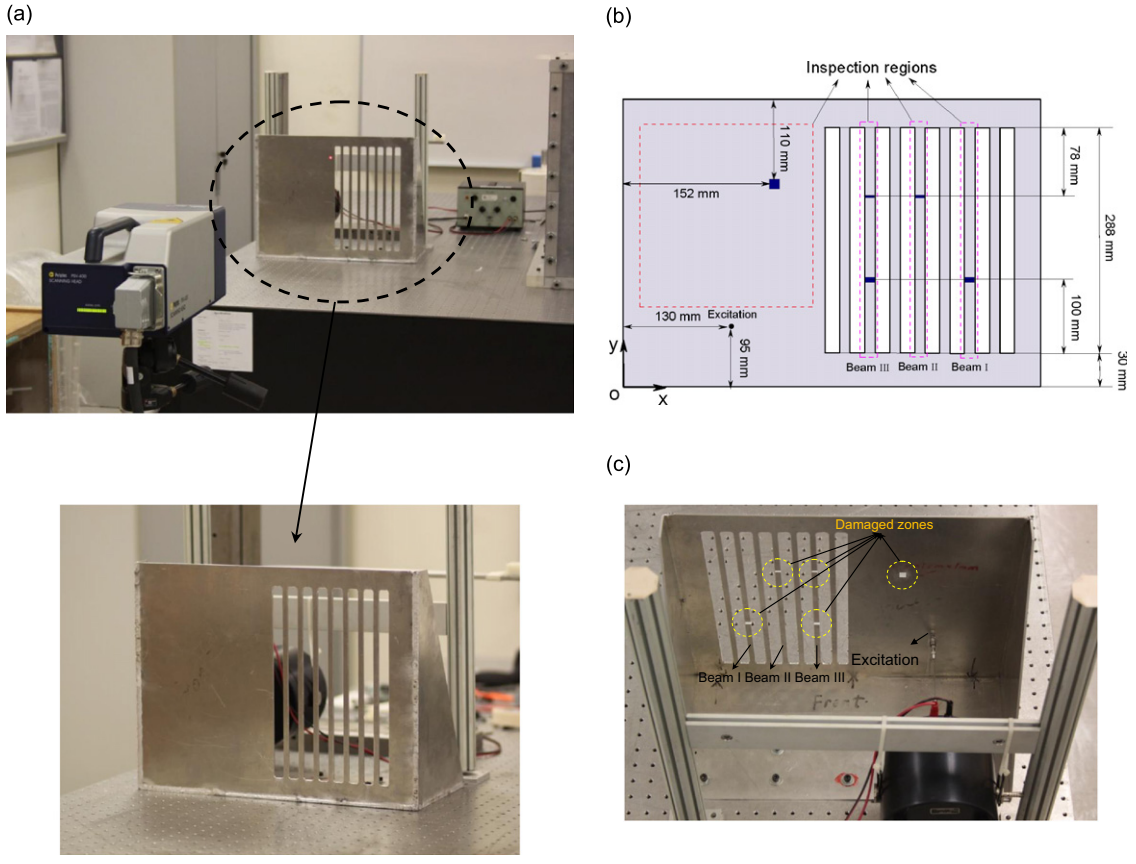

Fig. 14. Experimental application: (a) experimental setup (front view); (b) dimensions of the front panel and five damaged zones (back view); and (c) experimental setup (back view) ((c) and (d) also indicate location of the point-force excitation source).

NI distributions at a number of selected d_m/λ ($d_m/\lambda = 0.016$, 0.031, 0.047, 0.062, 0.076, 0.092, 0.123, 0.154, 0.185) for scenario B. This concurrent presentation of AD and NI curves is called 'AD–NI *curve*', in which the location of the intersection between two curves (denoted by p_o) in the ideally acceptable region (shadowed area in Fig. 9) suggests the most optimal d_m/λ, and with it satisfactory identification without relying on any signal de-noising treatment can be achieved. The AD–NI curve can simply be presented graphically against the ideally acceptable region in the same diagram, indicating the accuracy of different selection of d_m/λ. It is interesting to note that the above recommended configuration ($d_m/\lambda = 0.123$) based on the observation from Fig. 7(e) and (f) is very close to the location of p_o in Fig. 9, well demonstrating the effectiveness of AD–NI curves in selecting an optimal measurement configuration. In the contrast, other options lead to either low accuracy of finite difference calculation (*e.g.*, $d_m/\lambda = 0.185$, with identification results in Fig. 7(h)) or poor noise immunity (*e.g.*, $d_m/\lambda = 0.047$, with results in Fig. 7(b)).

3.3.3. Discussions on AD–NI curve

The position of p_o in the ideally acceptable region can be affected by a variety of factors, amongst which the level of measurement noise and the damage severity were explored.

3.3.3.1. Measurement noise. Letting the averages of ε_b^R and ε_b^I be zero and $\sigma\{\varepsilon_b^R\} = \sigma\{\varepsilon_b^I\} = 10^{-10}$ m in the background noise (defined by Eq. (15)), Fig. 10 exhibits the AD–NI curves for scenario B subject to different $\sigma\{\Delta w\}$ (from 1‰ to 10%) when $\sigma\{\Delta\varphi\} = 1^o$ (in Fig. 10(a)), and different $\sigma\{\Delta\varphi\}$ (from 0.1^o to 10^o) when $\sigma\{\Delta w\} = 1\%$ (in Fig. 10(b)), respectively. The increase in noise level is observed to shift the NI curve upwards (though the trend is not strictly monotonic), elevating the position of p_o in the ideally acceptable region, limiting the maneuvering margin for selecting an optimal measurement density, and thus making the detection more challenging. Allowing for this, a greater noise level requests a larger d_m/λ (*i.e.*, sparser measurement density), so as to enhance the noise immunity of the damage index; but this incurs reduction in accuracy of finite difference calculation. Based on observations from Fig. 10, 0.08–0.13 for d_m/λ (corresponding

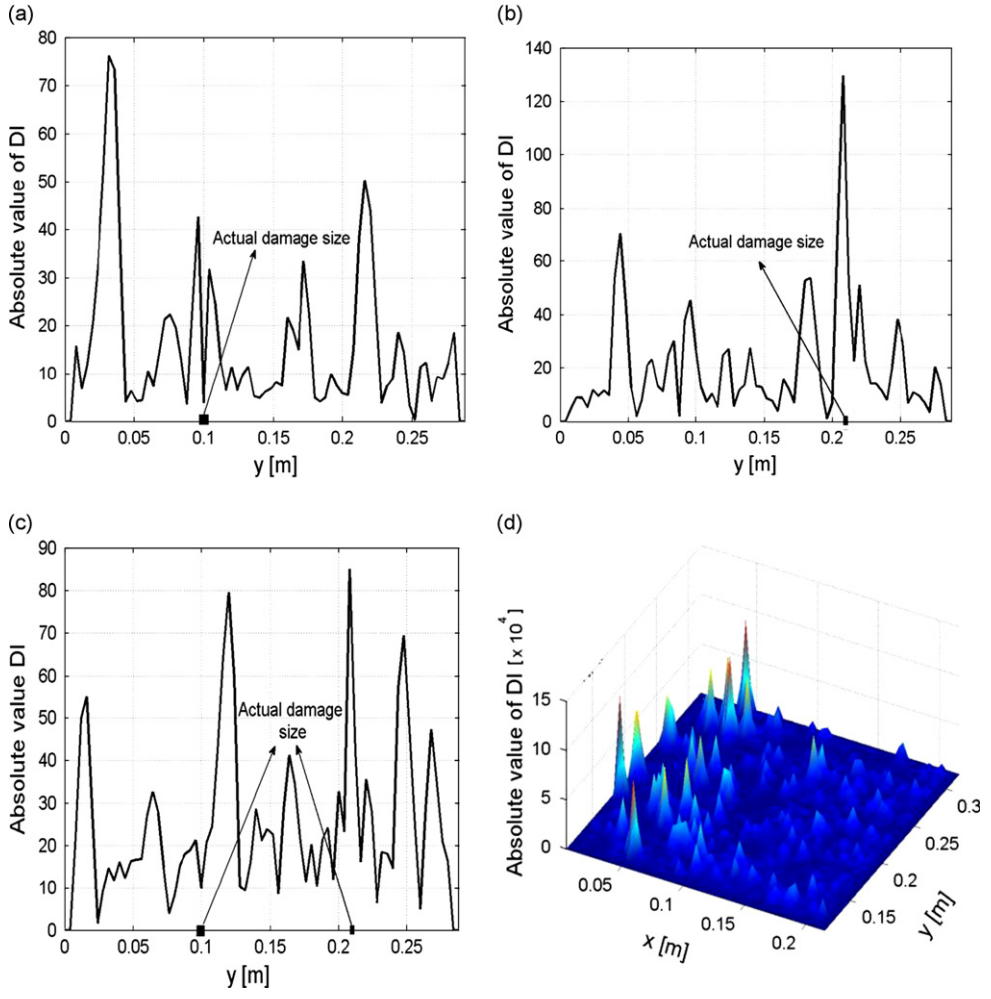

Fig. 15. Constructed damage index for beam components (a) I; (b) II; (c) III; and (d) plate component without using any de-noising treatment.

to 8–13 measurement points per λ for the current noise level) could be optimal. Contrarily, with less noise, the position of p_o moves towards the end with more measurement points. Generally speaking, around TEN measurement points per wavelength could be proposed as a rule of thumb for ascertaining an optimal measurement configuration. When the noise level exceeds a certain limit, p_o moves beyond the ideally acceptable region, and under such a circumstance the damage cannot be revealed if AMD is applied only, entailing application of LWF simultaneously. Such a conclusion is also applicable to more severe noise contamination up to 10% error in magnitude or 5° error in phase as demonstrated by the authors elsewhere [29].

3.3.3.2. Damage severity. For discussion, damage severity is diversified in a twofold way: different planar sizes and different thickness reductions. To facilitate generality of discussion, the damage size is defined with respect to wavelength λ (*i.e.*, ϑ/λ, where ϑ is the length of the longest edge of the damaged zone). Using scenario B under the same excitation condition and the same noise level ($\sigma\{\Delta w\}=1\%$ and $\sigma\{\Delta\varphi\}=1^{\circ}$) as example, Fig. 11 presents the AD–NI curves when the damaged zone has the same thickness reduction (one-third of that of the intact region) but is of four different sizes ($\vartheta/\lambda=0.028,\ 0.056,\ 0.113,\ 0.170$); Fig. 12 displays the AD–NI curves when the damaged zone remains the same planar size ($\vartheta/\lambda=0.056$) but has four different levels of thickness reduction (THR) (THR = 0.20, 0.25, 0.33, 0.50). It can clearly be noticed from both Figs. 11 and 12 that with the increase in damage severity (increase in either ϑ/λ or THR), the position of p_o migrates downwards in the ideally acceptable region (more phenomenal in Fig. 11), implying that a more severe damage impacts less stringent conditions on determination of an optimal measurement density, and vice versa.

It is pertinent to note that the edge of the square damaged zone in scenario B is roughly 4% of the wavelength only. The satisfactory detection accuracy has demonstrated that the proposed damage index is able to quantitatively characterize damage of small dimension by simply choosing an appropriate measurement configuration, without deploying any advanced signal processing treatment. This appealing attribute makes the proposed damage index outperform most traditional vibration-based methodologies (such as those based on the shift of eigen-frequencies, change in mode shape or damping properties) which can be less sensitive to damage before it reaches a conspicuous

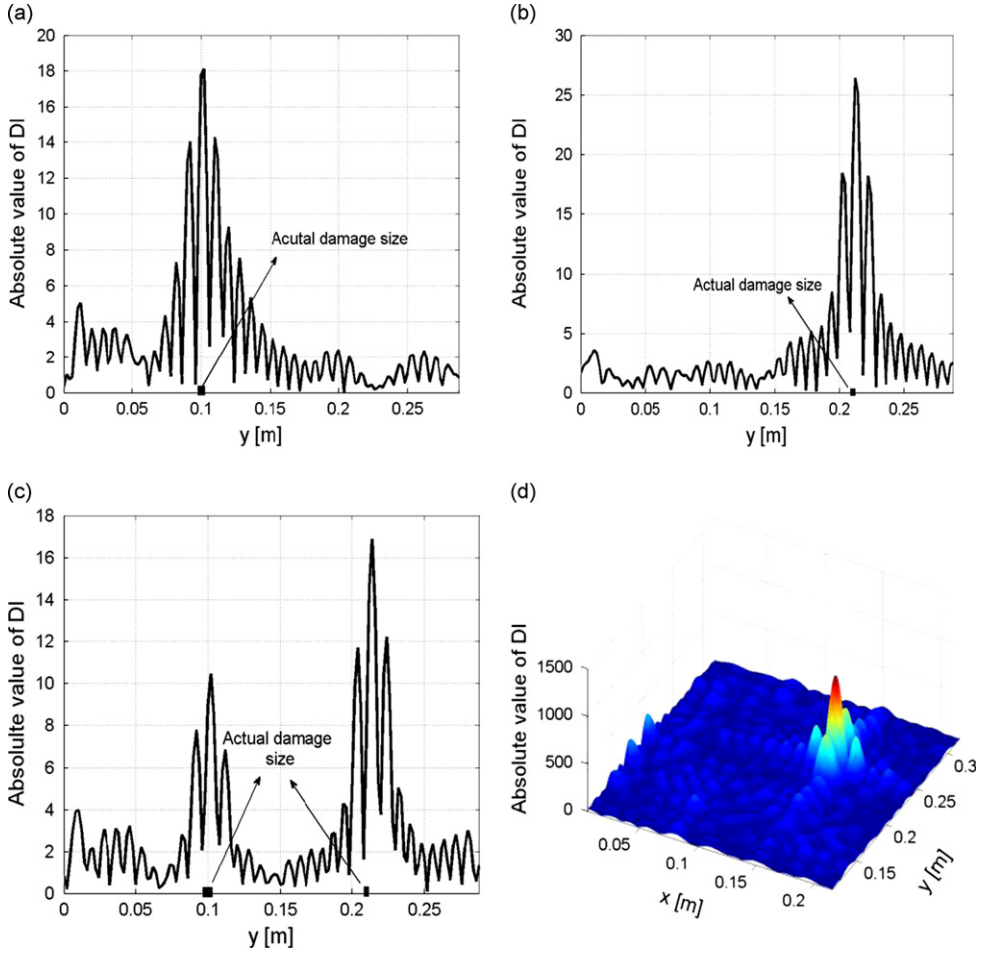

Fig. 16. Re-constructed damage index treated with LWF for beam components (a) I; (b) II; (c) III ($k_c=400$ rad/m); and (d) plate component ($k_c=250$ rad/m).

extent (*e.g.*, 10% of the characteristic dimension of the structure) or guided-wave-based approaches which show good detection capacity typically when the damage dimension is comparable to the wavelength of the selected wave mode.

4. Damage imaging and hybrid data fusion

The proposed $DI_{i,j}$ was further used as a two-dimensional field value at measurement point (i,j), enabling a two-dimensional damage imaging to intuitively present damage characterization results in a pixelated image. In such an imaging process, the inspection region is first meshed two-dimensionally and projected to a pixelated image with each pixel corresponding exclusively to a measurement point [30,31]. Exemplified by Fig. 7, the constructed image using $DI_{i,j}$ as the field value delivers an easily interpretable image, in which any singularity in the field value of a particular pixel indicates the existence of damage therein. Quantitative and detailed depiction of damage shape, size and severity can further be reached by locally canvassing those pixels with singularly elevated field values.

Owing to the flexibility of the approach, $DI_{i,j}$ can be constructed under a variety of measurement circumstances (*e.g.*, different excitation frequencies such as wideband excitation or even white noise excitation, different measurement densities, with or without use of LWF), contributing to a series of source images forming an image pool for information fusion. A hybrid data fusion algorithm was developed to amalgamate these source images, for minimizing noise influence along with LWF and AMD. Assuming the field value at pixel (i,j) can be obtained under K different measurement circumstances, denoted by $DI_{i,j-1}$, $DI_{i,j-2}$, $DI_{i,j-L}$, $DI_{i,j-L}$, $DI_{i,j-K}$ $(L=1,2,\ldots,K)$, the hybrid fusion algorithm is defined as

$$DI_{i,j\text{-hybrid}} = DI_{i,j\text{-arithmetic}} \cap DI_{i,j\text{-geometric}} \tag{20a}$$

where

$$DI_{i,j\text{-arithmetic}} = \frac{1}{K}\sum_{L=1}^{K} DI_{i,j-L} \tag{20b}$$

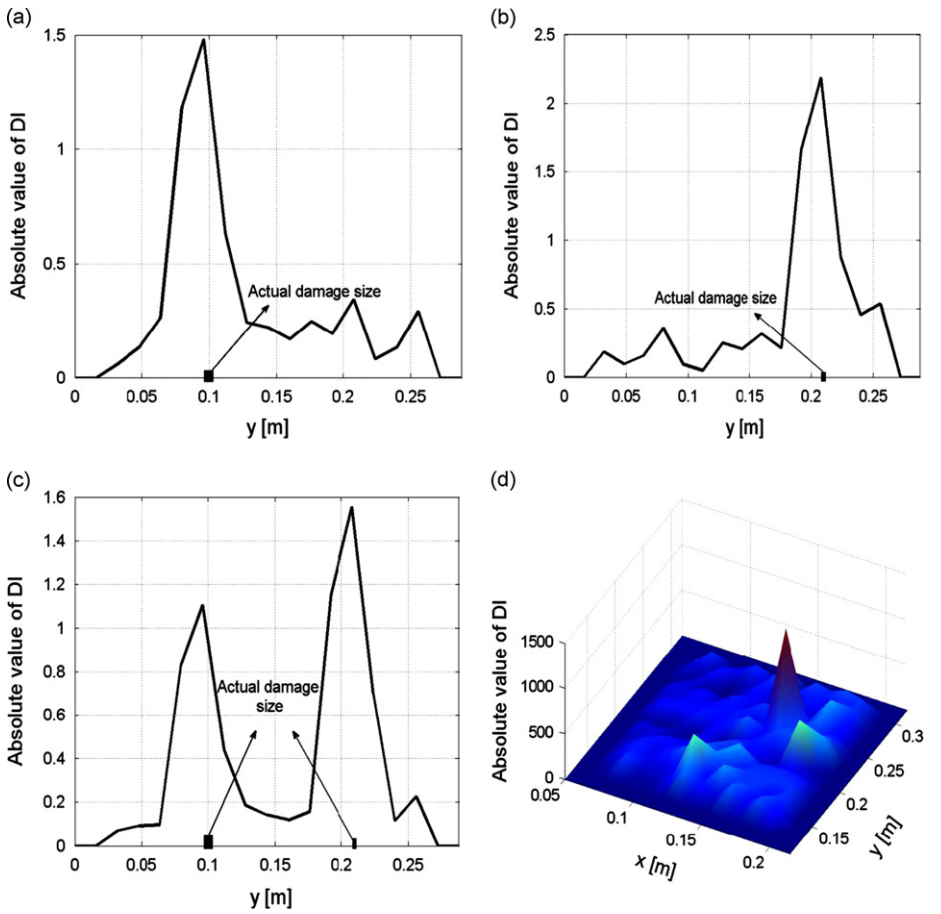

Fig. 17. Constructed damage index treated with AMD (nine measurement points per wavelength) for beam components (a) I; (b) II; (c) III; and (d) plate component.

and

$$\mathrm{DI}_{i,j\text{-geometric}} = \sqrt[\kappa]{\mathrm{DI}_{i-1}\cdot \mathrm{DI}_{i,j-2}\cdot \cdots \mathrm{DI}_{i,j-L}}\cdot \cdots \mathrm{DI}_{i,j-K} \tag{20c}$$

$\mathrm{DI}_{i,j\text{-hybrid}}$ is the ultimate field value at pixel (i,j) upon hybrid fusion. Development of such a hybrid fusion algorithm was motivated by the incentive to reap merits of individual data fusion schemes including the arithmetic and geometric fusion, so as to maximize the fusion efficiency with limited information sources [1]. The fusion achieves a compromise between the arithmetic and geometric fusion, by equally taking into account the perceptions from all source images whereas appropriately decentralizing their contributions; thus giving prominence to the salient features in common (*i.e.*, those pertaining to damage) and meanwhile suppressing less salient features in individuals (*e.g.*, measurement noise). For demonstration, Fig. 13 two- and three-dimensionally displays the ultimate image for scenario B obtained by fusing two source images (the noise-polluted source image in Fig. 6(b) treated with LWF and the one in Fig. 7(f)) using the hybrid fusion scheme. Although only two source images fused, largely enhanced precision has been achieved, to see the fused results outperform either of the source images in predicting location and shape of the damaged zone. Further improvement by fusing more source images can be anticipated, to be demonstrated in subsequent sections.

In addition, it is relevant to note that the resolution of the ultimate image is also subject to d_m, which should naturally be sufficiently small in order to explicitly depict damage of small dimension. However, as discussed in Section 3, d_m should be discreetly selected in line with the excitation frequency. If the AMD-based de-noising is adopted and a small d_m is opted for accommodating the above image resolution requirement, it is advisable to use a relatively high excitation frequency (thus relatively small λ), so as to keep an reasonably large d_m/λ to abate possible noise influence.

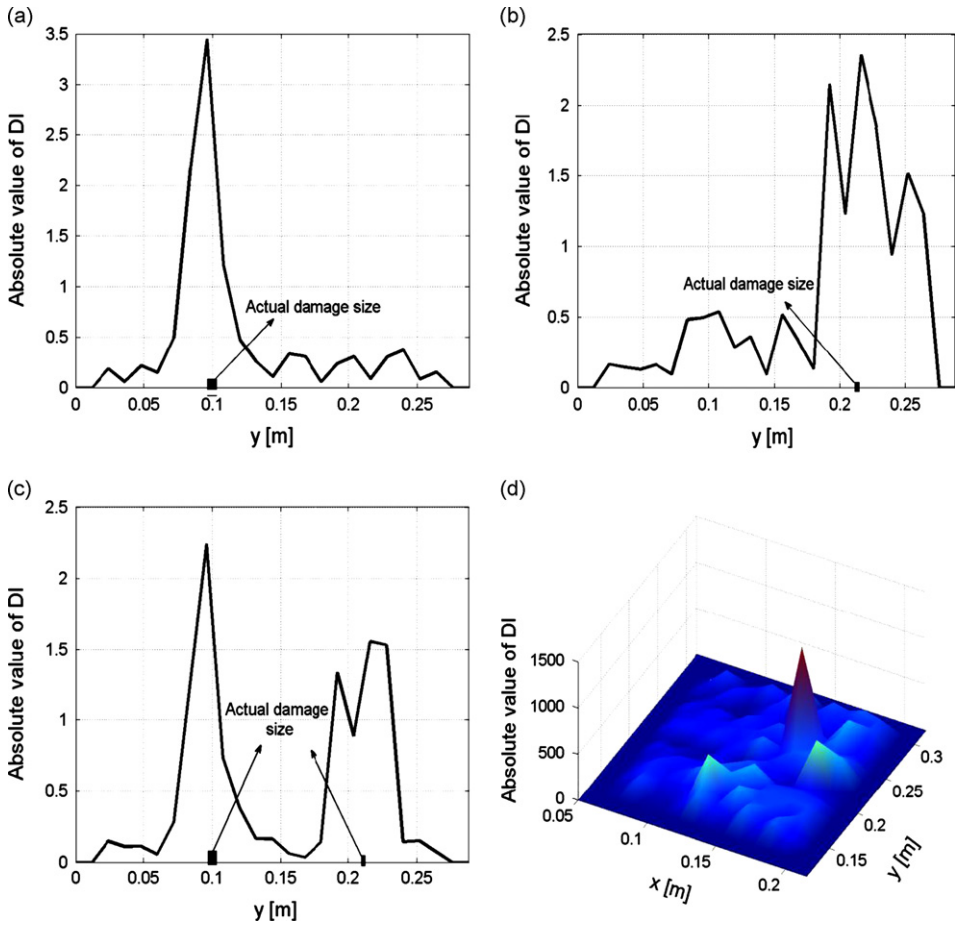

Fig. 18. Constructed damage index treated with AMD (twelve measurement points per wavelength) for beam components (a) I; (b) II; (c) III; and (d) plate component.

5. Application to multi-damage characterization in a plane structure

With the two damage indices defined over one- (Eq. (1)) and two-dimensional (Eq. (12)) domains, the detection framework is logically applicable to systems comprising beam and plate components simultaneously. In addition, the attribute of local canvassing warrants characterization of multi-damage.

In the application, a box-like structure was fabricated (Aluminum 6061, Young modulus: 68.9 GPa, mass density: 2.7 g/cm^3, and Poisson's ratio: 0.27), as shown in Fig. 14(a). The structure consisted of four (front, left, right and lower) panels with a uniform thickness of 3 mm, and the lower panel was fixed-supported on a testing table (NEWPORT® ST-UT2). The front panel (450×350 mm^2) was hollow-carved to configure seven parallel beam components (288 mm long, 8 mm wide and 3 mm thick each), with an interval of 12 mm. As shown in Fig. 14(b), multi-damage was introduced to the back surface of the front panel: a square damaged zone (1.4 mm thickness reduction) in the plate component, and four through-width notches (1.4 mm thickness reduction) in three beam components (in particular beam III containing two notches). The locations and planar dimensions of individual damage are indicated in Fig. 14(b). A harmonic point-force excitation through an electro-mechanical shaker (B&K® 4809) was applied to the back surface of the front panel (see Fig. 14(b) and (c)) with various frequencies (800, 1300, 1800 and 2300 Hz). Note that selecting a resonance frequency of the structure is not of necessity; actually it is preferable to apply this method at an off-resonance regime, so as to minimize the effect of system damping. Within the inspection region, the out-of-plane displacements were captured using a scanning Doppler laser vibrometer system (Polytec® PSV-400) at each measurement point on the intact surface of the front panel, opposite to which lay the multi-damage. The measurement setup is photographed in Fig. 14(a) and (c). $DI_{i,j}$ was constructed at each measurement point using Eq. (1) for the beam components and using Eq. (13) for the plate component.

The damage characterization results obtained using the imaging algorithm for three beam and plate components, at the excitation frequency of 1800 Hz as a representative, are displayed in Fig. 15. These results were obtained at a relatively high density of measurement points (73 measurement points along the beam component, and 61×61 across the inspection region of the plate component), without the use of LWF or AMD. To accommodate this measurement density, it took around 3 min to complete the scan for each beam component, while 1 h for the entire system. Strong noise influence was observed, preventing the approach delivering accurate damage characterization.

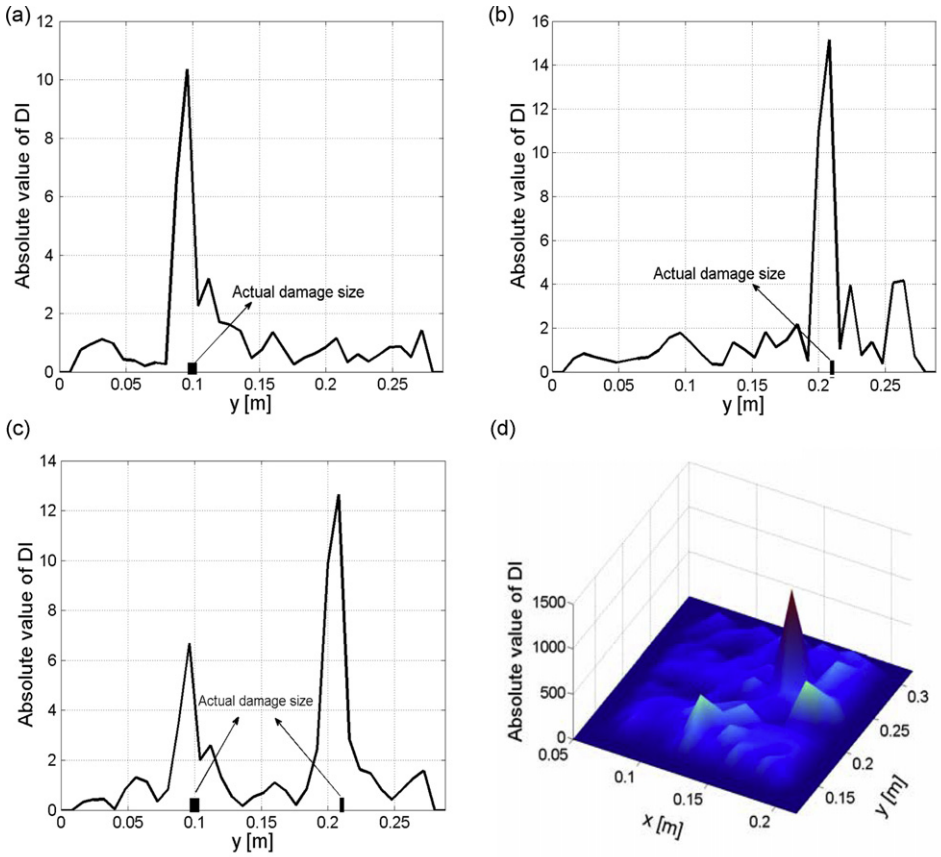

Fig. 19. Constructed damage index treated with AMD (fifteen measurement points per wavelength) for beam components (a) I; (b) II; (c) III; and (d) plate component.

LWF was applied alone by setting $k_c = 250\,\mathrm{rad}/m$ for the plate component and $k_c = 400\,\mathrm{rad}/m$ for three beam components in Eq. (16) (selection criterion for k_c detailed elsewhere [1]). The accordingly obtained results are shown in Fig. 16, clearly highlighting the location and rough size of all damage cases. Independent of LWF, AMD was applied with different measurement densities from 9 to 15 points per wavelength, and the results at several representative configurations are present in Figs. 17–19. As seen, the one with nine measurement points per wavelength (Fig. 17) is sufficient to warrant satisfactory identification for all damage cases in the structure, corroborating the conclusion drawn previously that the selection of around TEN measurement points per wavelength is able to strike a balance between accuracy of finite difference calculation and noise tolerance. It is also observed that a higher density (*e.g.*, 15 per wavelength in Fig. 19) contributes to a slightly improved accuracy, which can be attributed to the fact that the noise level in this application using laser vibrometer was actually low (typically less than 0.5%). Such a low level of noise entailed denser measurement configuration compared to the case discussed in the simulation (1% noise corruption was used in

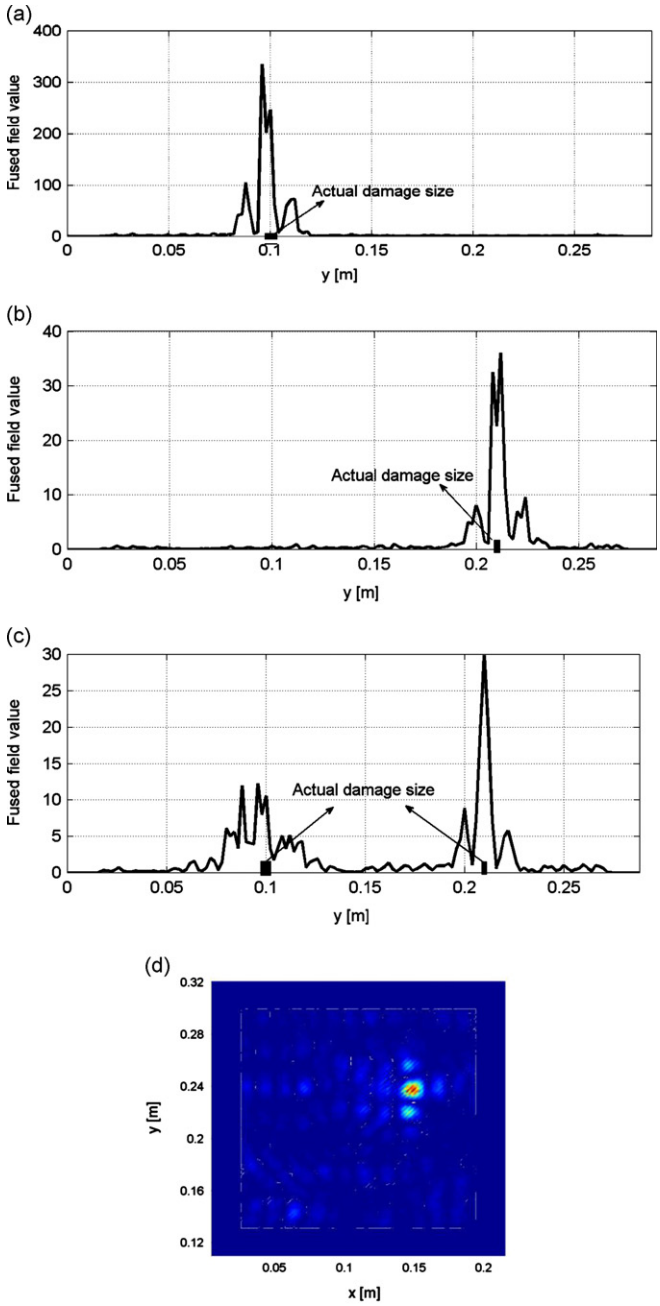

Fig. 20. Fused ultimate images for beam components (a) I; (b) II; (c) III; and (d) plate component.

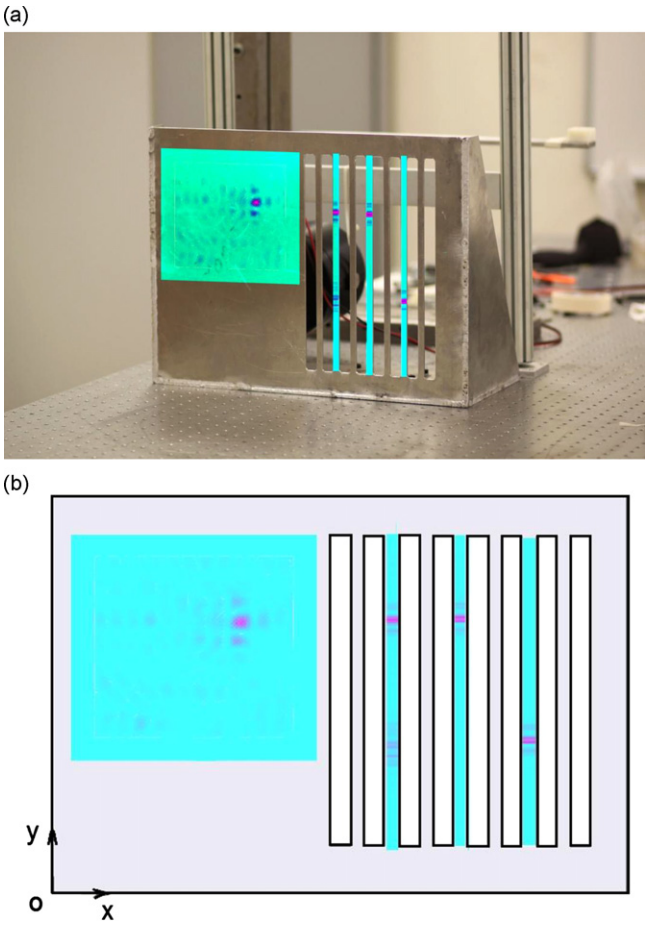

Fig. 21. (a) Three- and (b) two-dimensional damage image for the plane structure upon integration with photo of the structure.

simulation) from which the conclusion was reached. In addition, comparing two damage cases in beam III, Fig. 19(c), a smaller damaged zone incurs more prominent changes in field values compared with a greater one, accentuating that more severe damage does not necessarily lead to a greater field value (damage index), because, on top of the damage severity, the damage index is comprehensively subject to the distribution of internal bending forces and moments as discussed in Section 2.

In this application, various excitation frequencies and flexible choice of measurement configuration were used, leading to an image pool. With the hybrid fusion algorithm (Eq. (20)), Fig. 20(a)–(d) displays the fused ultimate images for three beam and plate components. With much enhanced recognizability, the fused results accurately and quantitatively depict all damage cases in the structure, including individual locations, shapes and sizes. To allow damage visualization for the entire structure, images for individual components were further integrated with the photo of the box-like structure, contributing to a three-dimensional damage image, in Fig. 21. Note that all the evidenced damaged zones are invisible from the surface on which the scan was conducted.

6. Conclusions

Deployed in a two-dimensional domain and based on the plate theory, a damage characterization framework by detecting the perturbation to local dynamic equilibrium was developed for plate-like components. A hybrid damage visualization strategy was established for systems comprising structural components of different types, various geometric parameters and diverse boundary conditions. To circumvent potential noise influence on identification accuracy, different de-noising techniques, including LWF, AMD and a hybrid data fusion algorithm, were proposed with their effectiveness demonstrated. LWF is able to screen out noise contamination in higher wavenumber region. Approximately TEN measurement points per wavelength can be seen as a practical rule to reach a compromise between detection accuracy and tolerance to measurement noise. Both numerical simulation and experimental application accentuated that the approach is able to characterize multiple damage in a quantitative manner under a noisy measurement condition. With the aid of an imaging approach, results can be presented intuitively in pixelated images. Benefiting from intrinsic

attributes of the damage index (no prerequisite for benchmarks, baseline signals, global models, additional excitation sources, pre-modal analysis nor prior knowledge on boundary), the proposed method, along with auxiliary de-noising tools, provides a flexible solution to the detection of multi-damage in complex systems comprising various structural components. Though scanning laser vibrometer was employed to capture vibration responses, the demand of a dense set of measurement points may dilute the practicability of the approach, entailing further improvement.

Acknowledgments

The authors wish to acknowledge the support given to them by the Hong Kong Polytechnic University (Research Grants A-PL08 and A-PL71). They are also grateful to the National Natural Science Foundation of China for a research grant (Grant no. 11272272).

References

[1] H. Xu, L. Cheng, Z. Su, J.L. Guyader, Identification of damage in structural components based on locally perturbed dynamic equilibrium, *Journal of Sound and Vibration* 330 (24) (2011) 5963–5981.
[2] H. Sohn, C.R. Farrar, F.M. Hemez, D.D. Shunk, D.W. Stinemates, B.R. Nadler, J.J. Czarnecki, A Review of Structural Health Monitoring Literature: 1996–2001, Los Alamos National Laboratory Report, LA-13976-MS, 2003.
[3] K. Worden, C.R. Farrar, G. Manson, G. Park, The fundamental axioms of structural health monitoring, *Proceedings of the Royal Society A* 463 (2007) 1639–1664.
[4] C.R. Farrar, D.A. Nix, W. Scott, S.W. Doebling, Vibration-based structural damage identification, *Philosophical Transactions of the Royal Society of London Series A* 359 (2001) 131–149.
[5] W. Fan, P. Qiao, Vibration-based damage identification methods: a review and comparative study, *Structural Health Monitoring: An International Journal* 10 (2011) 83–111.
[6] Y.S. Lee, M.J. Chung, A study on crack detection using eigenfrequency test data, *Computers and Structures* 77 (2000) 327–342.
[7] J.T. Kim, Y.S. Ryu, H.M. Cho, N. Stubbs, Damage identification in beam-type structures: frequency-based method vs. mode-shape-based method, *Engineering Structures* 25 (2003) 57–67.
[8] R.L. Mayes, Error localization using mode shapes-an application to a two link robot arm, *Proceedings of the 10th International Modal Analysis Conference*, San Diego, California, February 1992, pp. 886–891.
[9] A.K. Pandey, M. Biswas, M.M. Samman, Damage detection from changes in curvature mode shapes, *Journal of Sound and Vibration* 145 (2) (1991) 321–332.
[10] J. Chance, G.R. Tomlinson, K. Worden, A simplified approach to the numerical and experimental modeling of the dynamics of a cracked beam, *Proceedings of the 12th International Modal Analysis Conference*, Honululu, Hawaii, January 1994, pp. 778–785.
[11] V. Giurgiutiu, C.A. Rogers, Recent advancements in the electro-mechanical (E/M) impedance method for structural health monitoring and NDE, *Proceedings of SPIE on Smart Structures and Materials* 3329 (1998) 536–547.
[12] A.K. Pandey, M. Biswas, Damage detection in structures using changes in flexibility, *Journal of Sound and Vibration* 169 (1) (1994) 3–17.
[13] Y. Aoki, O. Byon, Goichi Ben, Damage detection of CFRP pipes and shells by using localized flexibility method, *Advanced Composite Materials* 10 (2001) 189–198.
[14] A.M. Yan, J.C. Golinval, Structural damage localization by combining flexibility and stiffness methods, *Engineering Structures* 27 (2005) 1752–1761.
[15] G. Kawiecki, Modal damping measurement for damage detection, *Smart Materials and Structures* 10 (2001) 466–471.
[16] Z. Su, X. Wang, L. Cheng, L. Yu, Z. Chen, On selection of data fusion schemes for structural damage evaluation, *Structural Health Monitoring: An International Journal* 8 (2009) 223–241.
[17] W. Ostachowicz, P. Kudela, P. Malinowski, T. Wandowski, Damage localisation in plate-like structures based on PZT sensors, *Mechanical Systems and Signal Processing* 23 (2009) 1805–1829.
[18] P. Fromme, P.D. Wilcox, M.J.S. Lowe, P. Cawley, On the development and testing of a guided ultrasonic wave array for structural integrity monitoring, *IEEE Transactions on Ultrasonics Ferroelectrics and Frequency Control* 53 (2006) 777–785.
[19] A. Raghavan, C.E.S. Cesnik, Review of guided-wave structural health monitoring, *The Shock and Vibration Digest* 39 (2007) 91–114.
[20] L. Wang, F.G. Yuan, Damage identification in a composite plate using prestack reverse-time migration technique, *Structural Health Monitoring: An International Journal* 4 (2005) 195–211.
[21] J.-B. Ihn, F.-K. Chang, Pitch-catch active sensing methods in structural health monitoring for aircraft structures, *Structural Health Monitoring: An International Journal* 7 (2008) 5–19.
[22] J.E. Michaels, T.E. Michaels, Guided wave signal processing and image fusion for in situ damage localization in plates, *Wave Motion* 44 (2007) 482–492.
[23] X. Zhao, H. Gao, G. Zhang, B. Ayhan, F. Yan, C. Kwan, J.L. Rose, Active health monitoring of an aircraft wing with embedded piezoelectric sensor/actuator network: I. Defect detection, localization and growth monitoring, *Smart Materials and Structures* 16 (2007) 1208–1217.
[24] M. Ruzzene, Frequency-wavenumber domain filtering for improved damage visualization, *Smart Materials and Structures* 16 (2007) 2116–2129.
[25] H. Sohn, D. Dutta, J.Y. Yang, M. DeSimio, S. Olson, E. Swenson, Automated detection of delamination and disbond from wavefield images obtained using a scanning laser vibrometer, *Smart Materials and Structures* 20 (2011) 045017. (10 pp.).
[26] P. Kudela, M. Radzieński, W. Ostachowicz, Damage visualization enhancement by the wave field filtering and processing, *Proceedings of SPIE (Smart Structures/NDE)*, San Diego, 11–15 March 2012, Paper 8347-53.
[27] K.F. Graff, *Wave Motion in Elastic Solids*, Oxford University Press, London, 1975.
[28] C. Pezerat, J.L. Guyader, Force analysis technique: reconstruction of force distribution on plates, *Acta Acustica United with Acustica* 86 (2000) 322–332.
[29] H. Xu, L. Cheng, Z. Su, Characterizing damage in plate structure based on local perturbance to dynamic equilibrium, *Proceedings of the eighth International Workshop on Structural Health Monitoring*, Stanford University, USA, September 2011, pp. 95–102.
[30] C. Zhou, Z. Su, L. Cheng, Probability-based diagnostic imaging using hybrid features extracted from ultrasonic Lamb wave signals, *Smart Materials and Structures* 20 (2011) 125005. (14 pp.).
[31] Z. Su, L. Cheng, X. Wang, L. Yu, C. Zhou, Predicting delamination of composite laminates using imaging approach, *Smart Materials and Structures* 18 (2009) 074002. (8 pp.).